

# Lawrence Berkeley National Laboratory

## Lawrence Berkeley National Laboratory

### Title

HEAT TRANSFER IN POROUS MEDIA WITH FLUID PHASE CHANGES

### Permalink

<https://escholarship.org/uc/item/8t42d4gt>

### Author

Su, Ho-Jeen.

### Publication Date

1981-06-01

Peer reviewed



# Lawrence Berkeley Laboratory

UNIVERSITY OF CALIFORNIA

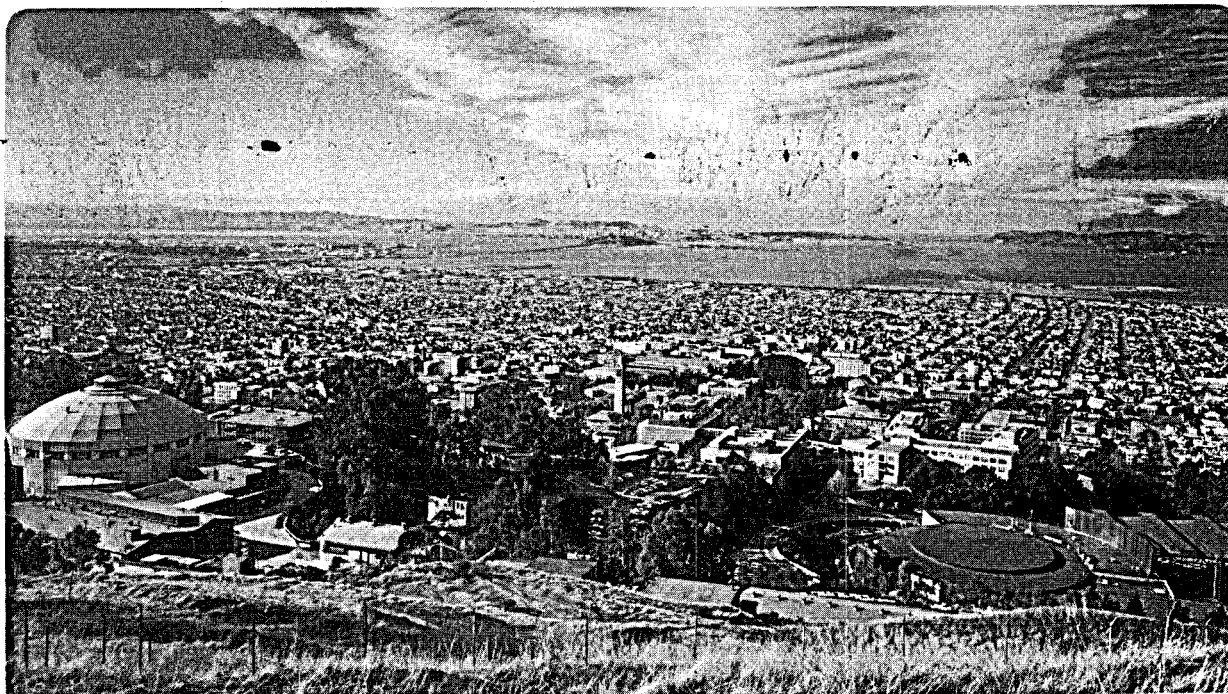
## EARTH SCIENCES DIVISION

**MASTER**

HEAT TRANSFER IN POROUS MEDIA WITH  
FLUID PHASE CHANGES

Ho-Jeen Su  
(Ph.D. thesis)

June 1981



#### **LEGAL NOTICE**

This book was prepared as an account of work sponsored by an agency of the United States Government. Neither the United States Government nor any agency thereof, nor any of their employees, makes any warranty, express or implied, or assumes any legal liability or responsibility for the accuracy, completeness, or usefulness of any information, apparatus, product, or process disclosed, or represents that its use would not infringe privately owned rights. Reference herein to any specific commercial product, process, or service by trade name, trademark, manufacturer, or otherwise, does not necessarily constitute or imply its endorsement, recommendation, or favoring by the United States Government or any agency thereof. The views and opinions of authors expressed herein do not necessarily state or reflect those of the United States Government or any agency thereof.

Heat Transfer in Porous Media with  
Fluid Phase Changes

Ho-Jeen Su

Ph.D. Thesis

June 1981

Earth Sciences Division  
Lawrence Berkeley Laboratory  
University of California  
Berkeley, CA 94720

DISCLAIMER

This book was prepared as an account of work sponsored by an agency of the United States Government. Neither the United States Government nor any agency thereof, nor any of their employees, makes any warranty, express or implied, or assumes any legal liability or responsibility for the accuracy, completeness, or usefulness of any information, apparatus, product, or process disclosed, or represents that its use would not infringe privately owned rights. Reference herein to any specific commercial product, process, or service by trade name, trademark, manufacturer, or otherwise, does not necessarily constitute or imply its endorsement, recommendation, or favoring by the United States Government or any agency thereof. The views and opinions of authors expressed herein do not necessarily state or reflect those of the United States Government or any agency thereof.

This research was supported by the Director, Office of Energy Research, Office of Basic Energy Sciences, Division of Engineering, Mathematics, and Geosciences of the U.S. Department of Energy under Contract W-7405-ENG-48.

Dear Sirs,  
I have the pleasure to inform you that your order for [illegible] has been received and is being processed.

Yours faithfully,  
[illegible]

[illegible]

[illegible]

[illegible]

[illegible]

[illegible]

Very truly yours,  
[illegible]  
[illegible]

# Heat Transfer in Porous Media with Fluid Phase Changes

Ho-Jeen Su

## Abstract


In heat transfer in partially liquid saturated porous media, a so-called "Heat Pipe Effect" may be observed. Experimental measurements of thermal conductivity of such systems may be strongly affected by the presence of this phenomenon. The heat pipe effect could greatly increase the heat transfer capacity of a porous medium by virtue of latent heat exchange.

A one-dimensional experimental apparatus was built to study the heat pipe phenomenon. Basically, it consists of a 25 cm long, 2.5 cm I.D. Lexane tube packed with Ottawa sand. The two ends of the tube were subjected to different temperatures, i.e., one above the boiling temperature and the other below. The tube was well insulated so that a uniform one-dimensional heat flux could pass through the sand pack. Presence of the heat pipe phenomenon was confirmed by the temperature and saturation profiles of the sand pack at the final steady state condition. A one-dimensional steady state theory to describe the experiment has been developed which shows the functional dependence of the heat pipe phenomenon on liquid saturation gradient, capillary

pressure, permeability, fluid viscosity, latent heat, heat flux and gravity.

Influence of the heat pipe phenomenon on wellbore heat losses was studied by use of a two-phase two-dimensional cylindrical coordinate computer model. A finite difference scheme was developed to solve a set of partial differential equations describing the process. The numerical results using different formation property parameters are presented. For shallow formations, the heat pipe effect could increase the wellbore heat losses by up to 50 percent compared with heat conduction alone. The heat pipe phenomenon is not likely to occur in deep formations where the higher formation pressure will prevent development of a two-phase region.

Approved:

  
\_\_\_\_\_  
Wilbur H. Somerton  
Chairman of Committee

## ACKNOWLEDGMENTS

The author wishes to thank his adviser, Professor Wilbur H. Somerton, for his guidance and encouragement. Thanks are also extended to Professor Ralph A. Seban and Professor Virgil E. Schrock for serving on the committee.

This research was supported in part by the Director, Office of Energy Research, Office of Basic Energy Sciences, Division of Engineering, Mathematics, and Geosciences of the U. S. Department of Energy under Contract No. W-7405-ENG-48.



CONFIDENTIAL

The following information is being furnished to you for your information only. It is not to be distributed outside your organization. This information is the property of the United States Government and is loaned to you. It is to be used only for the purposes for which it was provided and is not to be retransmitted, copied, or otherwise disseminated. If you are not the intended recipient, you should not disseminate, distribute, or copy this information. If you have received this information in error, you should notify the sender immediately by telephone or in writing.

CONFIDENTIAL

## TABLE OF CONTENTS

	<u>Page</u>
ACKNOWLEDGMENTS	iii
LIST OF FIGURES	vi
LIST OF TABLES	ix
I. INTRODUCTION	1
II. ONE DIMENSIONAL STEADY STATE THEORY	6
II.1 Literature Review	6
II.2 Mechanism of Heat Pipe Phenomenon	11
II.3 Development of One-Dimensional Steady State Theory	19
III. ONE DIMENSIONAL EXPERIMENT	23
III.1 Previous Experimental Work	23
III.2 Experimental Apparatus	28
III.3 Experimental Procedure	31
III.4 Experimental Results	33
III.5 Comparisons of Theoretical Development with Experimental Results	43
IV. NUMERICAL SIMULATION OF WELLBORE HEAT LOSSES	49
IV.1 Introduction	49
IV.2 Mathematical Modeling	52
IV.3 Numerical Formulation for Wellbore System	58
IV.4 Verification of Numerical Model	65
IV.5 Numerical Results	70
IV.6 Applications	87
V. CONCLUSIONS	90
NOMENCLATURE	92

REFERENCES	94
APPENDIX A: DERIVATION OF TRANSFORMATION EQUATIONS	98
APPENDIX B: CALCULATION OF OVERALL HEAT TRANSFER COEFFICIENT	101

## LIST OF FIGURES

### Figure

- 1.1 Thermal conductivity of partially water-partially water vapor saturated Ottawa sand.
- 1.2 Conceptual model for heat pipe phenomenon in porous media.
- 2.1 Schematic diagram of the heat pipe.
- 2.2 Conceptual configuration of a two fluid phase system in a porous medium.
- 2.3 Configuration of thermodynamic equilibrium at a curved surface.
- 3.1 Simple schematic illustration of thermal conductivity measurement apparatus.
- 3.2 Example of temperature and liquid saturation profiles from an experiment.
- 3.3 Temperature distributions in partially saturated wick-transition zone.
- 3.4 Schematic of one dimensional experimental apparatus.
- 3.5 Temperature profile of Ottawa sand pack.
- 3.6 Temperature profile of Ottawa sand pack.
- 3.7 Temperature profile of Ottawa sand pack.
- 3.8 Temperature profile of Ottawa sand pack.
- 3.9 Example of resistivity measurement results.
- 3.10 Calculated saturation profile.
- 3.11 Temperature profiles at different time steps - experimental and calculated.
- 3.12 Steady state temperature profile of numerical results compared with experimental data.
- 4.1 Configuration of the wellbore surrounding.
- 4.2 Comparison of calculated pressure profiles with experimental data.

- 4.3 Comparison of calculated liquid saturation profiles.
- 4.4 Temperature history before evaporation starts.
- 4.5 Temperature and saturation histories of grid cell (1,1) for the standard case.
- 4.6 Saturation variation of grid point (1,4)
- 4.7 Temperature and saturation histories of grid cell (1,1) for the case C ( $k = 0.05$  darcys).

## LIST OF TABLES

### Table

- |      |  |
|------|--|
| 3.1  | List of experimental tests.  |
| 4.1  | Specifications for overall heat transfer coefficient calculation.              |
| 4.2  | Input specifications for 2-D simulation.                                       |
| 4.3  | Input specifications for simulation of Stanford experiment.                    |
| 4.4  | Numerical results at 42.53 hours.  |
| 4.5  | Numerical results at 45.77 hours.  |
| 4.6  | Numerical results at 302.8 hours.  |
| 4.7  | Water pressure distribution at 302.8 hours.                                    |
| 4.8  | Numerical results of case A at 48.71 hours.                                    |
| 4.9  | Numerical results of case B at 44.4 hours.                                     |
| 4.10 | Numerical results of case C at 45.77 hours.                                    |
| 4.11 | Numerical results of case D at 45.83 hours.                                    |
| 4.12 | The maximum possible depths of a two-phase zone developed around the wellbore. |

MEMORANDUM

11/15/54

TO: SAC, NEW YORK

FROM: SA [Name], NEW YORK

SUBJECT: [Subject]

[Text]

[Text]

[Text]

[Text]

[Text]

[Text]

[Text]

[Text]

[Text]

[Text]

[Text]

[Text]

[Text]

[Text]

[Text]

[Text]

[Text]

[Text]

[Text]

[Text]

[Text]

[Text]

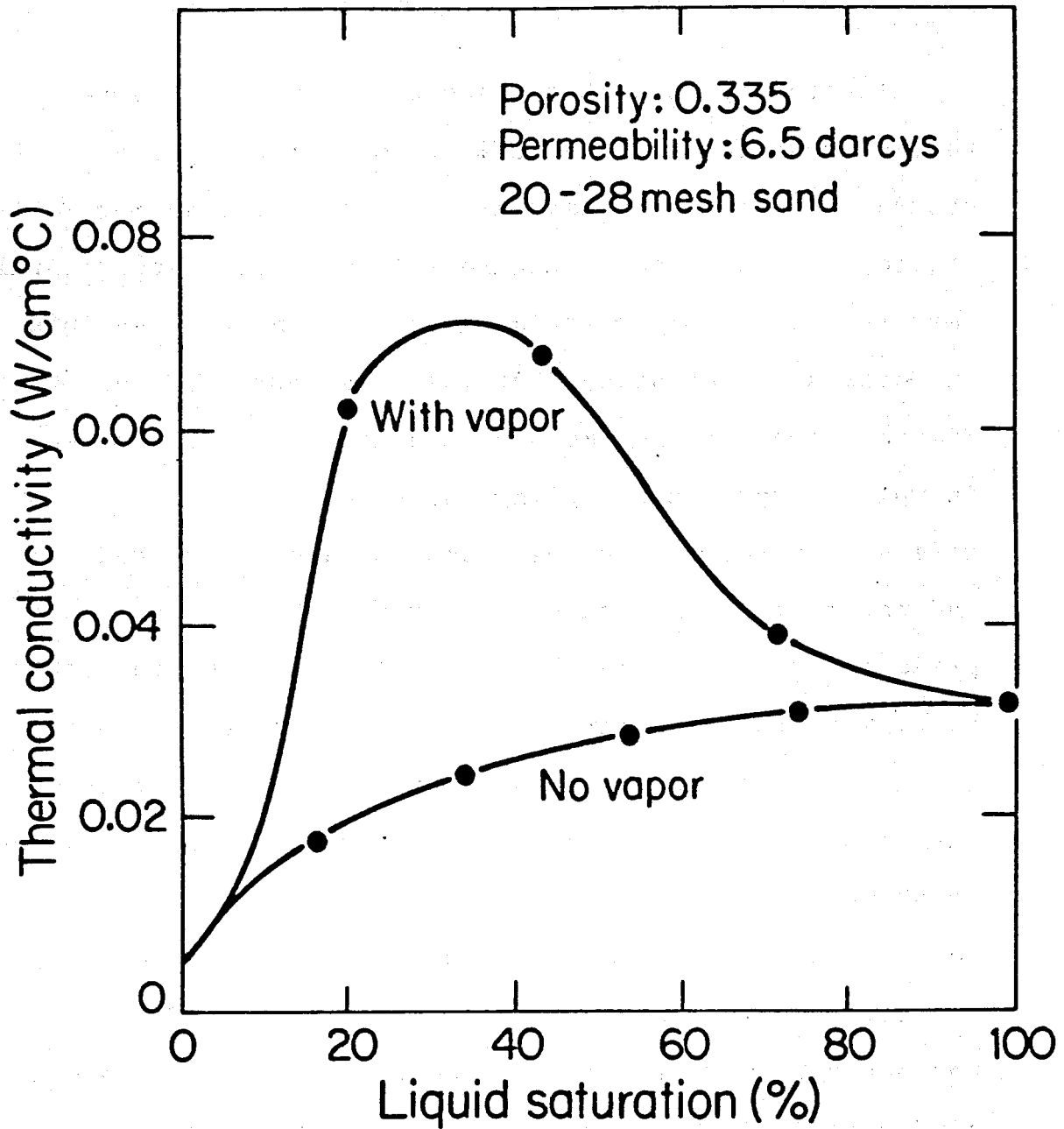
[Text]

## CHAPTER I. INTRODUCTION

In earlier work, Gomaa and Somerton (1) observed that the apparent thermal conductivity of partially liquid saturated sand can be several times larger than for fully liquid saturated sand. Figure 1.1 shows the experimental results from a comparator apparatus which was described in Gomaa's dissertation (2). The lower curve of the figure represents the measured values of the experiments in which temperature settings were below the boiling condition. Therefore the test samples mainly included air and water, the vapor existed only for the partial vapor pressure of the thermodynamic equilibrium. On the other hand, when the temperature settings of the experiment were raised to the range above the boiling temperature, the trend of the experimental results was greatly changed as shown by the upper curve.

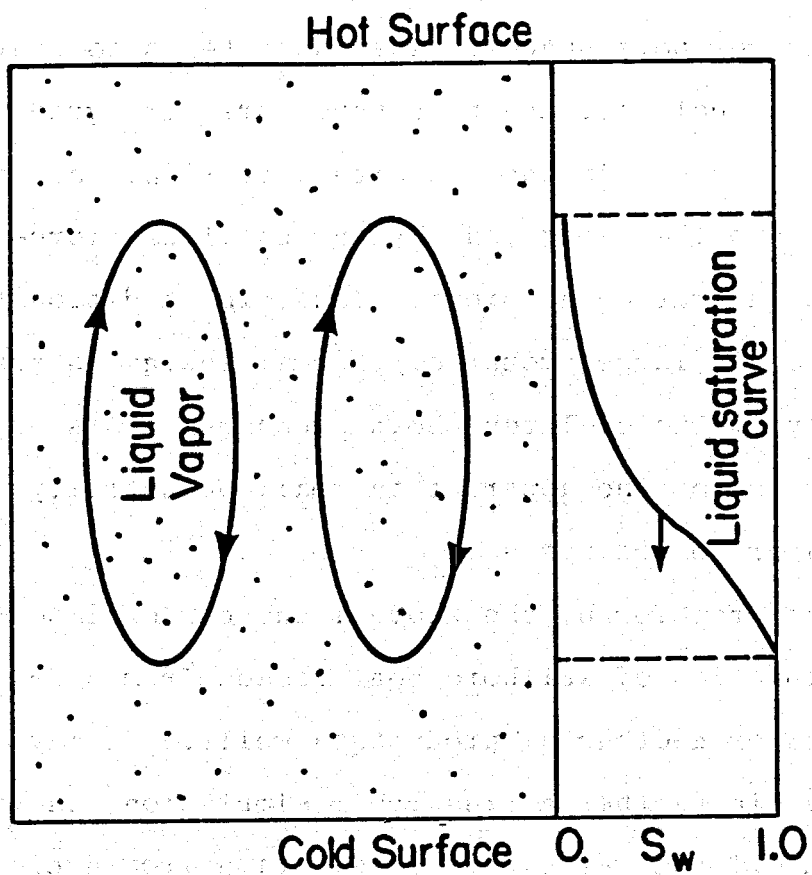
Gomaa and Somerton applied the so-called "heat pipe concept in porous media" (3) to explain the difference between the two sets of experimental results. As shown in Figure 1.2, a core sample saturated with water is subjected to two different temperatures, one above the boiling temperature and the other below. Suppose that a pressure regulator is installed at the bottom surface to allow fluid flow out of the system. Gradually some water will be displaced by the vapor generated near the hot surface, then the core sample becomes a water-vapor





XBL 7910 - 4555

Figure 1.1 Thermal conductivity of partially water-  
partially water vapor saturated Ottawa sand.  
(1)



XBL 7910-4551A

Figure 1.2 Conceptual model for heat pipe phenomenon in porous media.

saturated porous system. The water and the vapor are not separated into distinct zones, but both of the phases are distributed through the entire porous system. Inside the pore space the water is the wetting phase and is adjacent to the solid surface and in the fine pore spaces. The vapor phase is the non-wetting phase and is in the center of the larger pore spaces. The vapor tends to travel towards the cold surface by a vapor pressure gradient and condenses there. In the opposite direction, the water is brought into the vapor zone by the capillary force due to a liquid saturation gradient. Thus, in addition to heat conduction, a large amount of thermal energy is transported by virtue of latent heat exchange. This explains the increase of the apparent thermal conductivity for a water-vapor porous system.

Heat transfer by the above means can be important in the calculation of wellbore heat losses from steam injection or geothermal production wells. It may also be important in geothermal reservoir simulation, thermal enhanced oil recovery, heat dissipation from nuclear waste disposal stored in water bearing formations, underground storage of hot fluids from power plants, or other thermal processes involving liquid saturated porous media.

The purpose of this study is to gain a further understanding of the heat pipe phenomenon in porous media and to give a quantitative analysis of its magnitude. A one dimensional experiment was designed to measure the temperature and saturation profiles of a 25.4 cm long,

5.08 cm in diameter sand pack. This experiment is designed to confirm the heat pipe phenomenon in a long tube and investigate the principal mechanism. Based on the mass balance principle and Darcy's law, a simple analytic equation was obtained for a steady state, linear porous system. The numerical results obtained using the equation were compared with experimental data.

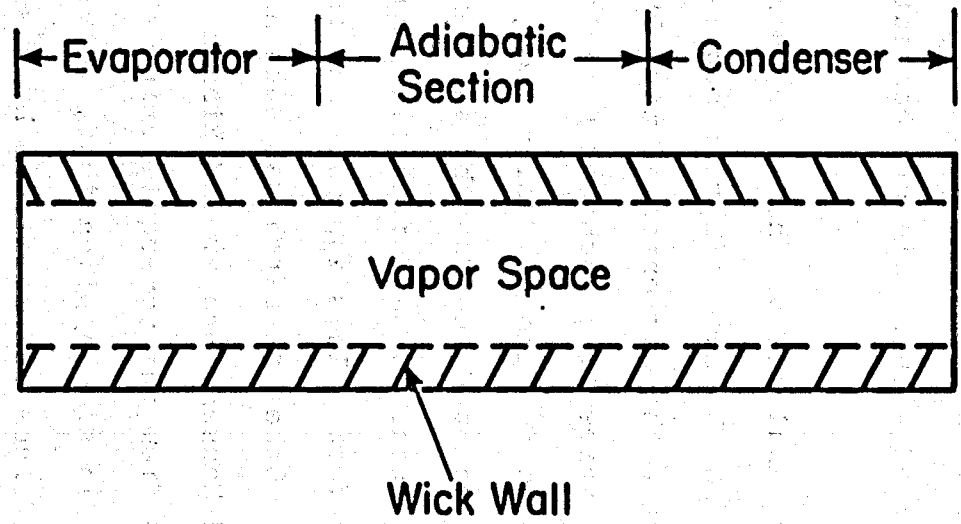
All of the applications are transient and multi-dimensional problems. Thus a set of simultaneous, coupled partial differential equations for energy, momentum, and continuity need to be solved. There is no general solution for all of the possible applications, and the wellbore heat losses problem was selected as an example to illustrate the methodology of the numerical simulation which includes the heat pipe phenomenon in porous media. The significance of the heat pipe phenomenon is shown from the numerical results.

## CHAPTER II. ONE DIMENSIONAL STEADY STATE THEORY

### II.1. Literature Review

The heat pipe concept was first introduced by Grover, Cotter and Erickson (4) who studied the behavior of very high conductance systems. As illustrated in Fig. 2.1, a heat pipe is usually a slender pipe lined on the inside surface with a liquid saturated wick of very highly porous and permeable material. The hollow channel in the center, surrounded by the wick, is for the vapor passage. The pipe is divided into three sections: evaporator, adiabatic section, and condenser. The liquid is evaporated in the evaporator section which is heated by an external source. The vapor travels to the condenser section cooled by an external heat sink and condenses there. The capillary force returns the condensate to the evaporation section and the cycle continues. The adiabatic section lies between the other sections and is insulated. Many investigators have worked on applying the heat pipe concept and improving its performance. Some representative works were by Cotter (5), Tien (6), and Sun (7).

The earlier research work on thermal behavior of porous systems which display capillary phenomena probably started at least fifty years ago in the field of Soil Science. Boyoucos (8), Winterkorm (9), and Taylor and Carazza (10) concluded that moisture movement in porous



XBL 814-667

Figure 2.1 Schematic diagram of the heat pipe.

media under a temperature gradient can be coupled with the local evaporation and condensation conditions. Liquid can be evaporated into vapor at a warmer part, and vapor will move towards the colder part due to diffusion or pressure gradient and will condense there. Simultaneously, there is liquid flow by a capillary driving force associated with a moisture content gradient.

The quantitative analysis of the above phenomenon has been developed through many different approaches at later times. Following the conventional way, Philip and de Vries (11) and de Vries (12) combined Darcy's law for liquid flow, Fick's law for gas diffusion flow, Fourier's law for heat conduction, and the mass balance and energy balance relations to obtain a set of partial differential equations in general form. This approach has included the presence of air. Other researchers, such as Valchar (13), Cary (14), and Hansen, Breyer and Riback (15), have tackled this problem from the non-equilibrium thermodynamics viewpoint. In some applications, they can simplify the set of force-flux relations by Onsager reciprocal relations of phenomenological coefficients and mass and energy conservation law. Hansen, Breyer and Riback (15) have applied this technique to a linear steady-state thermal conductivity measurement process and a simple linear equation was obtained:

$$J_q = L_{qq} \nabla \ln T \quad (2.1)$$

where  $J_q$  refers to heat flux,  $L_{qq}$  is the phenomenological coefficient and  $\nabla \ln T$  is the driving force. From the experimental results, they observed that the same value of  $L_{qq}$  was obtained for the same values of temperature and liquid content in different experiments even though the temperature and liquid gradients are different. This supports the validity of Eq. (2.1). Furthermore, it implies that the total heat flux, the sum of conductive heat transfer and latent heat transport, can be calculated with the known phenomenological coefficient and temperature profile. However, the values of the phenomenological coefficients are the characteristics of the porous systems and must be empirically determined.

Gomaa (2) proposed both a macroscopic model and a microscopic model for analysis of a steady state linear vapor-water porous system, and the following solution was obtained for both models:

$$\lambda_{ap} = \lambda_{HP} + \lambda = \frac{2\bar{m} h_{fg} L^2}{3(T-T_s)(1-\phi S_v)} + \lambda \quad (2.2)$$

where  $\bar{m}$  is the average mass evaporation or condensation rate,  $h_{fg}$  is the latent heat, and  $L$  is the length of the system.  $T$  and  $T_s$  denote the local temperature and saturation temperature,  $\phi$  is porosity and  $S_v$  is vapor saturation. The vapor saturation is defined as the percentage of the pore space occupied by the vapor phase.  $\lambda$  is the thermal conductivity if there were no heat pipe effect, while  $\lambda_{HP}$  represents the contribution of the heat pipe effect to the apparent thermal conductivity,  $\lambda_{ap}$ . In the above



derivation the following assumptions were made:

1. The vapor and water temperatures are different at the same cross section.
2. The local evaporation or condensation rate is linear along the length of the porous system.
3. The variation of vapor saturation throughout the porous system is neglected, i.e., the local vapor saturation equals the average value of vapor saturation of the entire system.
4. The thermal conductivity of vapor is assumed negligible, and the energy balance is only applied to the liquid-solid matrix.
5. Total heat flux =  $-\lambda \nabla T$  is assumed at the end points, i.e., the phase change effect at these points is neglected.

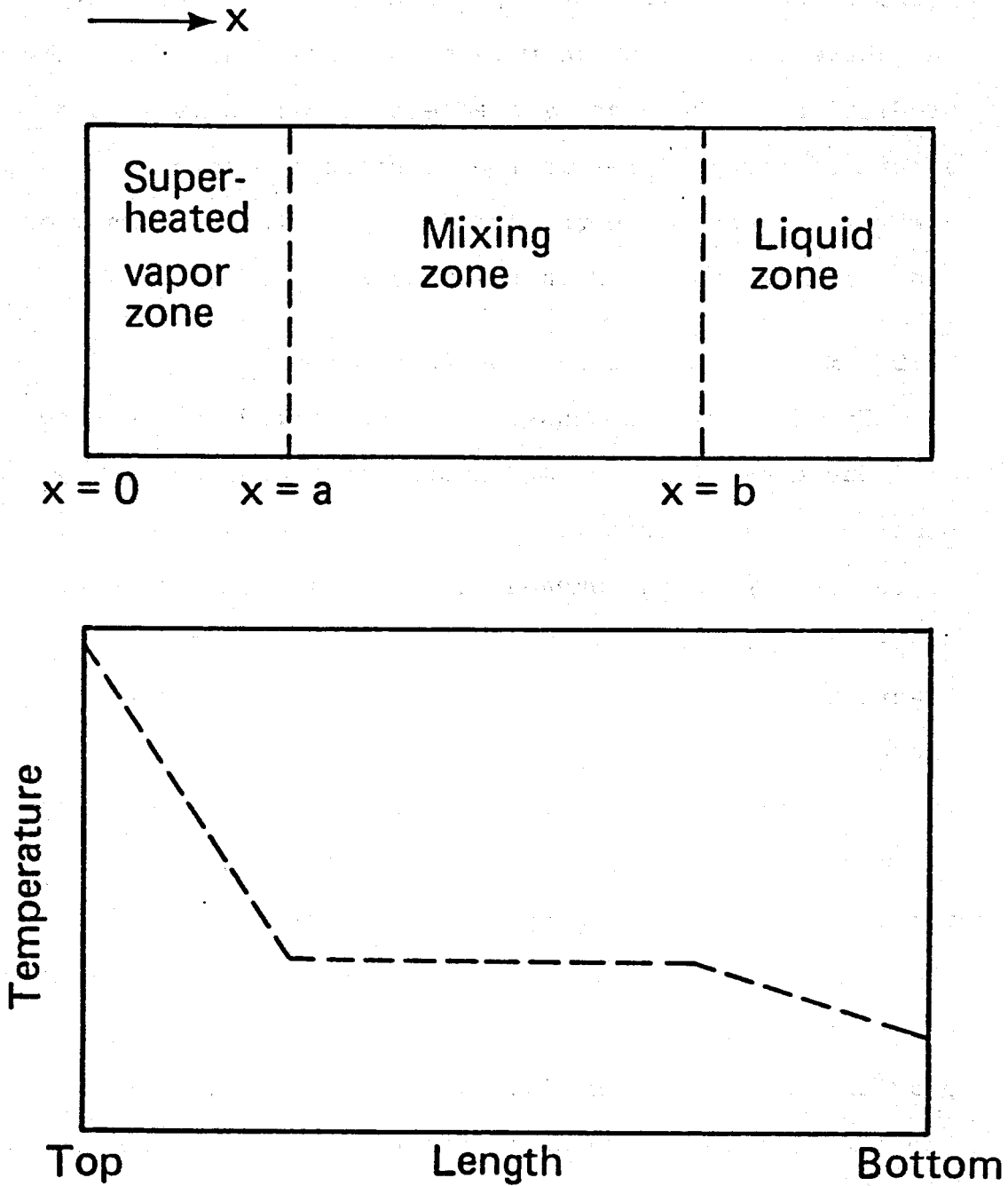
Obviously, these assumptions are overly simplified.

Gomaa also ran regression analysis for the experimental results of the thermal conductivity measurements of partially liquid saturated core samples. He obtained a correlation formula for the heat pipe effect in terms of average liquid saturation of the core sample, absolute permeability, viscosities of vapor and liquid phases, latent heat and porosity. Note that the driving force of the heat pipe effect is the capillary pressure gradient due to the liquid saturation gradient but is not included in the correlation formula. In the absence of capillary

pressure and liquid saturation gradient from the analysis, the above correlation formula is probably only valid for prediction of the heat pipe effect in partially liquid saturated core samples in the specific apparatus. However, it does give the order of importance of many of the variables involved in the process.

## II.2. Mechanism of Heat Pipe Phenomenon

The following discussion is restricted to the case of a one-dimensional porous system in which the steady state heat pipe effect is occurring. The main mechanism of the heat pipe phenomenon in a one-dimensional porous system is the counterflow of the liquid and its vapor. Figure 2.2 shows a conceptual configuration of a two-phase system in porous media. The vapor is generated at the zone where a temperature higher than or equal to the boiling temperature exists, and then the vapor travels towards the colder zone by a vapor pressure gradient. This vapor pressure gradient can result from a temperature gradient in the mixing zone, although the temperature gradient may be very small. The vapor will condense at the intersection between the mixing and the liquid zones. At the same time, there is a counterflow of liquid due to a liquid pressure gradient. The existence of the liquid pressure gradient will be explained later in this section in discussion of the capillary pressure concept. Note that the fluid flow discussed above is also influenced by the gravity. To include the gravity effect, the



XBL 7910 - 4552

Figure 2.2 Conceptual configuration of a two fluid phase system in a porous medium

pressure gradient,  $\nabla P$ , should be replaced by  $(\nabla P - \rho \hat{g})$ .

The following assumptions and restrictions are needed before any further discussion of the heat pipe phenomenon in porous media:

1. There is no air present in the porous system. Only a single working liquid and its vapor exist in the pore spaces such as water and water vapor.
2. The porous structure is homogeneous. The porosity and absolute permeability are assumed to be uniform throughout the system.
3. The fluid flow rates, temperature, pressure and liquid saturation are uniform over the same cross section. For example, there are no liquid islands in a partially liquid saturated zone.
4. The liquid is the wetting phase and its vapor is the non-wetting phase.
5. The two phases are assumed to be continuous in the mixing zone.
6. The flow paths for both phases are tortuous.
7. The liquid and its vapor phase have the same temperature at the same location, i.e., they are in thermodynamic equilibrium. Evaporation or condensation may occur at the two ends of the mixing zone. Thus the mass flow rates for the two phases must be equal but opposite in direction in order to satisfy the mass

conservation law

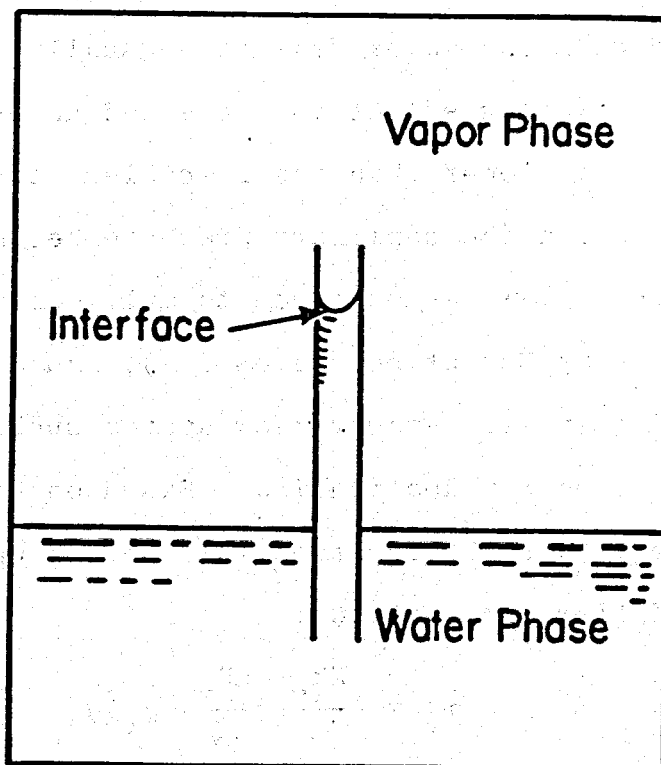
$$|m| = \hat{m}_v = -\hat{m}_w \quad (2.3)$$

8. The fluid flow rates for both phases are assumed to be small enough to be within the laminar flow region. Thus Darcy's law can be applied to both phases.
9. Inside the porous system the solid material has the same temperature as the fluid phases. There is no heat transfer across the interface of the solid material and the fluid phases.

For a partially liquid saturated porous media, there is a capillary pressure between the two phases:

$$\begin{aligned} P_c &= P_{\text{non-wetting}} - P_{\text{wetting}} \\ &= P_v - P_w = \sigma \left( \frac{1}{r_1} + \frac{1}{r_2} \right) \end{aligned} \quad (2.4)$$

where  $\sigma$  is the interfacial tension between the two phases, and  $r_1$  and  $r_2$  are the principal radii of curvature of the interface. The radii will be determined by the water content in the porous medium, therefore, the capillary pressure is a function of liquid saturation. Two phase flow in porous media is associated with the thermodynamics of curved surface. If the two phases are assumed to be in thermodynamic equilibrium, then they exist at the same temperature but at different pressures. As shown in Fig. 2.3, Keenan (16) discussed that both the water pressure and the vapor pressure at equilibrium



XBL 814-668

Figure 2.3 Configuration of thermodynamic equilibrium at a curved surface. (16)

conditions will be lower than for the case of a flat surface if the interface between the two phases is a concave surface towards the water phase. Thus, the water pressure will decrease substantially as the water saturation decreases. The effect on the vapor pressure is not as great since the vapor density is negligible compared with the water density. Usually the vapor pressure lowering effect is neglected unless the water saturation is lower than the so-called "irreducible" value at which the capillary pressure becomes very large.

Darcy's law was extended to multi-phase flow in oil reservoirs by Muskat and Meres (17), and it has been adopted for a water-vapor flow system such as in the geothermal energy application. Based on Darcy's law, the mass flow rates for the fluid phases can be calculated by the following equations:

$$\hat{m}_v = -\frac{Kk_v}{\nu_v} \left( \frac{dP}{dx} - \rho_v \hat{g} \right) \quad (2.5)$$

$$\hat{m}_w = -\frac{Kk_w}{\nu_w} \left( \frac{dP}{dx} - \rho_w \hat{g} \right) \quad (2.6)$$

where  $K$  = absolute permeability,

$k_v, k_w$  = relative permeabilities,

$p$  = pressure,

$\rho$  = density,

$\nu$  = kinematic viscosity,

$\hat{x}$  = distance in vector form.

Values of relative permeabilities, fractions of the absolute permeability, used in the above equations, are

determined empirically. Although relative permeabilities are functions of pressure, temperature and liquid saturation, their values are usually expressed as functions of liquid saturation only.

In petroleum engineering, the "irreducible water saturation" is defined as the water saturation at which the water flow becomes negligible. For the vapor phase, the "critical gas saturation" is defined in the same manner. In this work these saturation values are defined as the values at which the discontinuity is developed. For example, the water flow due to a water pressure gradient is not likely if the water in the pore spaces is not interconnected.

There is a lack of relative permeability data for the water-vapor system. In geothermal reservoir analysis, the data for a gas-water or gas-oil system are used for a water-vapor system. Chen, Council and Ramey (18) have reported a large difference in relative permeability values between an air-water system and a vapor-water system for the same porous structure. Furthermore, the relative permeability values are empirically determined in a parallel multi-flow experiment which is in contrast to the counterflow pattern in this work. Therefore, the relative permeability values for application in heat pipe analysis need future investigation.

The above discussion applies to flow behavior in the mixing zone. Some consideration needs to be given to the heat transfer mechanisms in the superheated zone



and the liquid zone. The following argument is not rigorously verified and should only be viewed as a possible explanation of the phenomena occurring in these zones. The water transported through the mixing zone evaporates as it enters the superheated vapor zone. It is assumed that the evaporation occurs at the interface between the superheated zone and the mixing zone. The evaporation increases the vapor pressure inside the superheated zone due to the difference between the specific volumes of the two phases, causing some of the vapor to flow into the mixing zone. The above becomes a steady state process if the exit pressure is held constant. The water saturation in the superheated zone may become equal to zero or to some value below the irreducible water saturation. Hence heat convection by water movement in the vapor zone is not possible. Heat convection by vapor movement is assumed to be very small compared to heat conduction in the vapor zone. Radiation can be neglected if the temperature is less than  $400^{\circ}\text{C}$  (19). Therefore, heat conduction is the dominant heat transfer mechanism in the superheated zone. Thus the temperature profile in the superheated zone will be a straight line. This may be observed from the experimental results shown in Fig. 3.3 and Fig. 3.5. A similar argument can be applied to the liquid zone. If the hotter surface is not at the top of the system, some strong natural convection motion may be induced in these two zones. This then becomes a two-dimensional problem which is not

considered at this time.

### II.3. Development of One-Dimensional Steady State Theory

Based on the assumptions and arguments in the above section, a simple equation can be derived for the heat pipe effect in a one-dimensional steady state situation. The following theory is only for the mixing zone portion of a porous system which may also include a superheated vapor zone and a liquid zone.

Combining Eqs. (2.3) through (2.6) and simplifying gives:

$$\hat{m}_v = |m| = \frac{K}{\left(\frac{\nu_w}{k_w} + \frac{\nu_v}{k_v}\right)} \left[ -\frac{dP_c}{dx} - \hat{g}(\rho_w - \rho_v) \right] \quad (2.7)$$

This is the governing flow equation for the heat pipe effect in a linear, closed porous system in the absence of air, and it illustrates the functional relationship between heat pipe effect and parameters such as permeability, viscosities, capillary pressure, and gravity.

If the capillary pressure is assumed to be a function of liquid saturation only, then

$$\hat{m}_v = \frac{K}{\left(\frac{\nu_w}{k_w} + \frac{\nu_v}{k_v}\right)} \left[ \left(-\frac{dP_c}{dS}\right) \Big|_S \frac{dS}{dx} - \hat{g}(\rho_w - \rho_v) \right] \quad (2.8)$$

where  $\left(-\frac{dP_c}{dS}\right) \Big|_S$  is the capillary pressure gradient with respect to saturation at a certain value of saturation.

The integral form of the above equation is

$$S_b - S_a = \int_a^b \frac{\hat{m}_v}{K} \left( \frac{\nu_w}{k_w} + \frac{\nu_v}{k_v} \right) + \hat{g}(\rho_w - \rho_v) \frac{1}{\left(-\frac{dP_c}{dS}\right) \Big|_S} d\hat{x} \quad (2.9)$$

or

$$b - a = \int_{S_a}^{S_b} \left( - \frac{dP_c}{dS} \right) \Big|_S \cdot \left[ \frac{1}{\frac{\hat{m}_v}{K} \left( \frac{\nu_w}{k_w} + \frac{\nu_v}{k_v} \right) + \hat{g}(\rho_w - \rho_v)} \right] dS \quad (2.10)$$

where b and a can be any two arbitrary points within the heat pipe phenomenon region.

If the mass flow rate is specified and all the fluid properties are known, the liquid saturation profile can be calculated from Eq. (2.8) provided that one of the boundary values of liquid saturation is given. Under the same conditions, Eq. (2.10) implies that the length of the two-phase mixing zone can be evaluated if the saturation values at the two end points are given.

If there is no or very small temperature gradient in the heat pipe phenomenon region, as shown in the experimental data of the next Chapter, then the heat flux can be predicted from the following analysis: Integrating Eq. (2.8) over the entire length of the mixing zone gives:

$$\int_c^d \hat{m}_v d\hat{x} = \int_{S_c}^{S_d} \frac{K}{\left( \frac{\nu_w}{k_w} + \frac{\nu_v}{k_v} \right)} \left( - \frac{dP_c}{ds} \right) \Big|_s ds - \int_c^d \hat{g}(\rho_w - \rho_v) d\hat{x} \quad (2.11)$$

where c and d denote the end points. Assuming there is no heat loss from this linear system, then the heat flux will be constant through the system as will the vapor

and water mass fluxes. Thus,

$$\begin{aligned}
 Q &= \hat{m}_v h_{fg} = \bar{m} h_{fg} \\
 &= \frac{K}{L} \int_{S_c}^{S_d} \frac{1}{\left(\frac{v_w}{k_w} + \frac{v_v}{k_v}\right)} \left(-\frac{dP_c}{ds}\right) \Big|_s ds \\
 &\quad - \int_c^d \hat{g}(\rho_w - \rho_v) dx \tag{2.12}
 \end{aligned}$$

where  $L$  is the total length of the mixing zone. The average mass flux is  $\bar{m}$  and  $Q$  is the heat flux. The first term in the right-hand side of the above equation is always a positive value, but the sign of the second term depends on the relative direction between gravity and heat flux. For a given length of the mixing zone, the maximum heat flux will be expected if gravity is opposite in direction to heat flux and the saturation values at the end points are at irreducible water and critical gas saturations. On the other hand, the heat flux would be eliminated if the two terms in the right-hand side were to cancel each other. This is not likely to occur in real systems.

The above equation may be useful for a fully porous heat pipe design, i.e., no hollow channel between the wick lining. For example, if the heat flux, the length of the heat pipe, and the fluid properties in the porous medium are specified, then the saturation values at both ends can be estimated by a trial and error technique using Eq. (2.12). The saturation profile can then be calculated from Eq. (2.8). The amount of liquid to be

contained inside the pipe can thus be calculated.

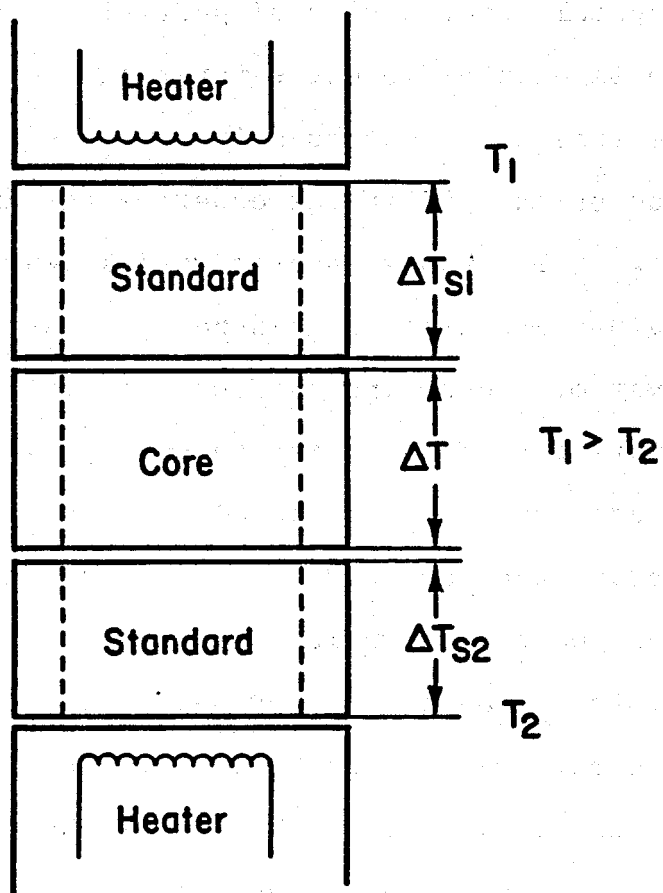
The above analysis is restricted to the simple linear steady state case. Other applications of the heat pipe phenomenon in porous media require solution of a set of partial differential equations as described in Chapter IV.

## CHAPTER III. ONE-DIMENSIONAL EXPERIMENT

### III.1. Previous Experimental Work

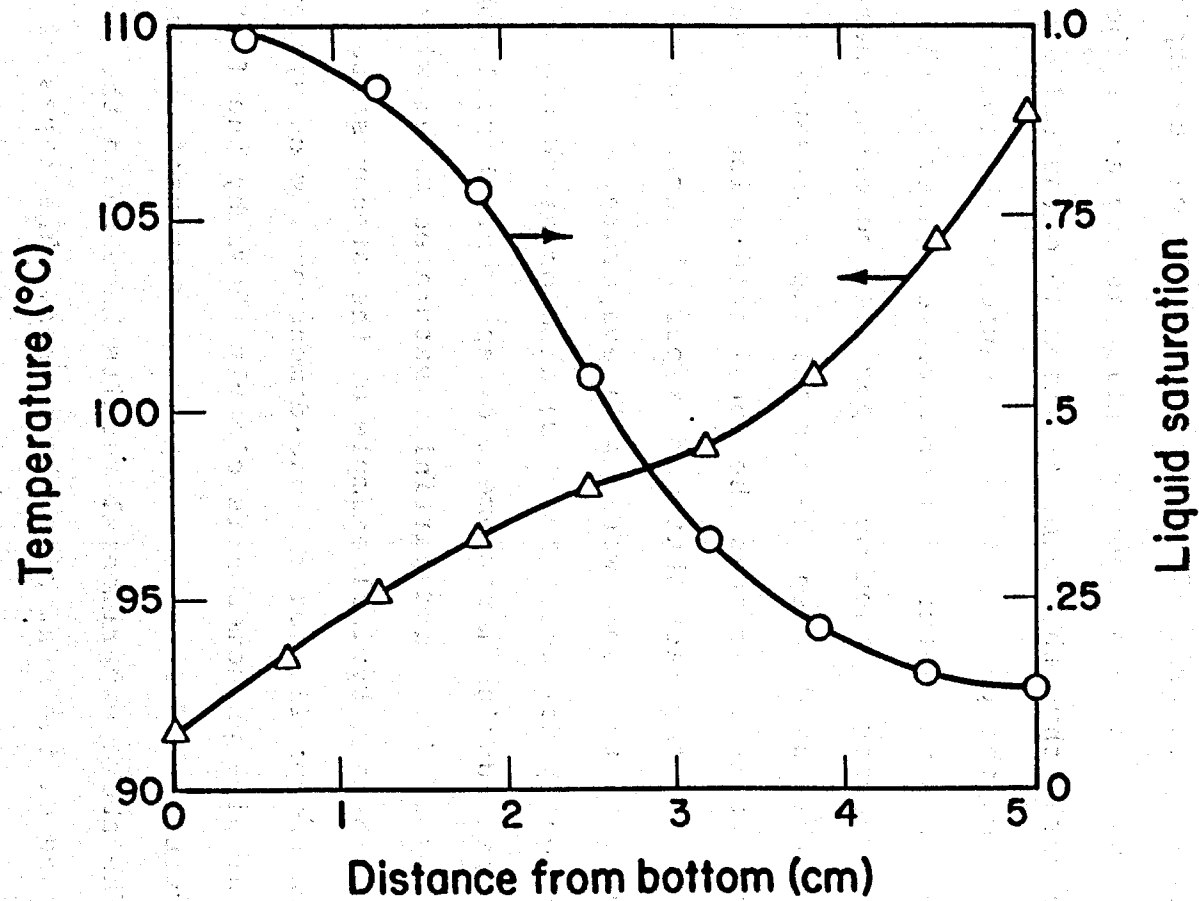
Gomaa (2) has made a number of measurements of the thermal conductivity of partially liquid saturated porous media with different saturating fluids such as brine, heptane and Stoddard solvent. A schematic diagram of the stack used in the experimental apparatus is shown in Fig. 3.1. Two standards with known thermal conductivity values are used to measure the heat flux through the system. According to Fourier's law, the thermal conductivity of the core can be calculated by dividing the heat flux by the ratio of the temperature difference across the core and the height of the core. This experiment does not provide information on the temperature distribution and liquid saturation distribution inside the core sample which data are needed for a thorough investigation of the heat pipe phenomenon in porous media.

Hansen, Breyer and Riback (15) used the X-ray method to determine liquid saturation distribution along a core sample. Thermocouples recorded the temperatures within the porous media at quarter inch intervals along a two inch thick core sample. One set of data was presented as shown in Fig. 3.2 from an experiment on glass beads at 61 percent average water saturation and 1.82 atm. total gas pressure. The gas phase included both air and water vapor. Note that the system pressure is above the



XBL 818-3472

Figure 3.1 Simple schematic illustration of thermal conductivity measurement apparatus (2)



XBL 818-3473

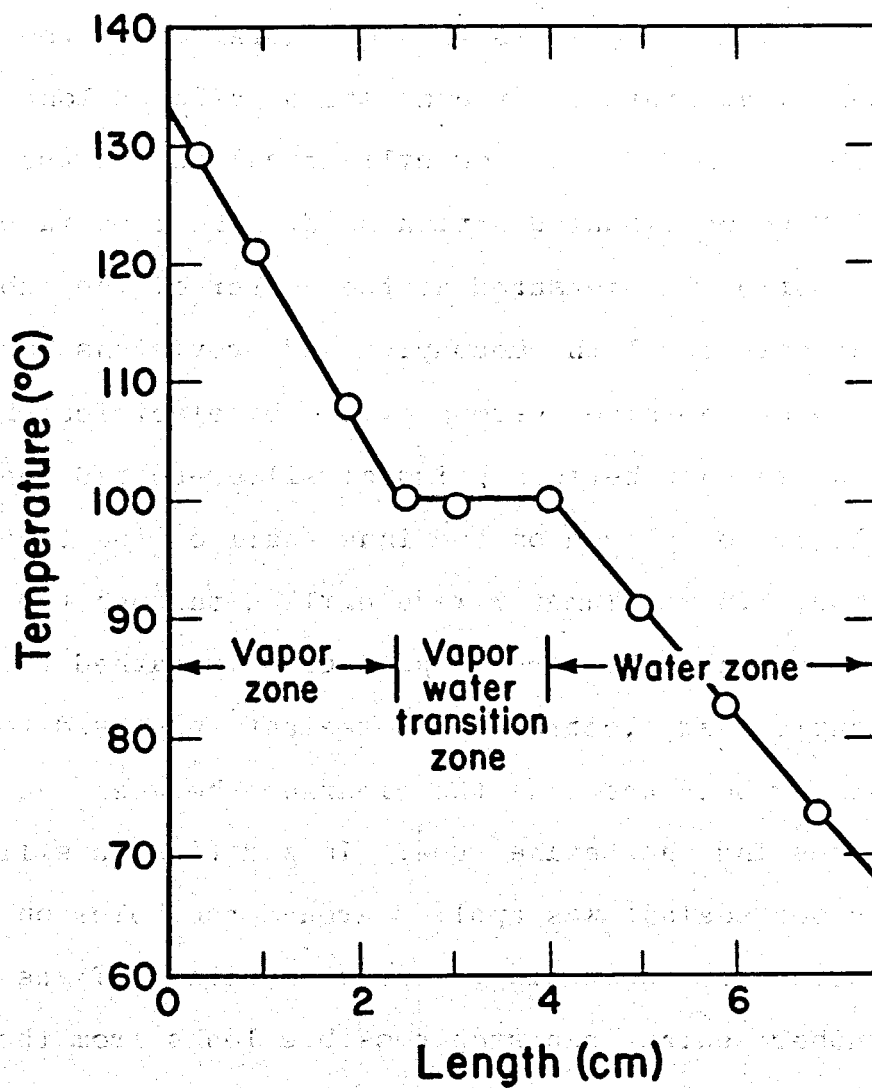
Figure 3.2 Example of temperature and liquid saturation profiles from an experiment (15),  $p_p = 1.82$  atm.



saturation pressure at the maximum system temperature, hence the evaporation rate at the warmer part is not very high. The heat pipe phenomenon occurs even though the system temperature was well below the corresponding boiling temperature. The reason for this can be explained as follows. The vapor concentration is higher at the warmer part, thus the vapor diffuses into the colder part. When the partial vapor pressure at the colder part exceeds the saturation pressure of water at the local temperature, then some vapor will condense there. On the other hand, when the partial vapor pressure at the warmer part is lower than the local saturation pressure value due to the fact that some vapor diffuses into the colder part, then some water will evaporate.

Recently Kar and Dybbs (19) also observed the heat pipe effect during measurement of apparent thermal conductivity of fully and partially saturated metal wicks. Figure 3.3 is a typical example of the steady state temperature profile of the one-dimensional wick system. The heat pipe phenomenon is clearly shown by the flat temperature profile at the vapor-water transition zone.

The above experimental results have shown the existence of the heat pipe phenomenon. The types of porous media used in the last two experiments are not similar to the porous media found in natural underground systems. Also many characteristics of the porous media, such as capillary pressure and relative permeabilities, were not presented in their papers. Hence, further



XBL 818-3474

Figure 3.3 Temperature distributions in partially saturated wick-transition zone (19)

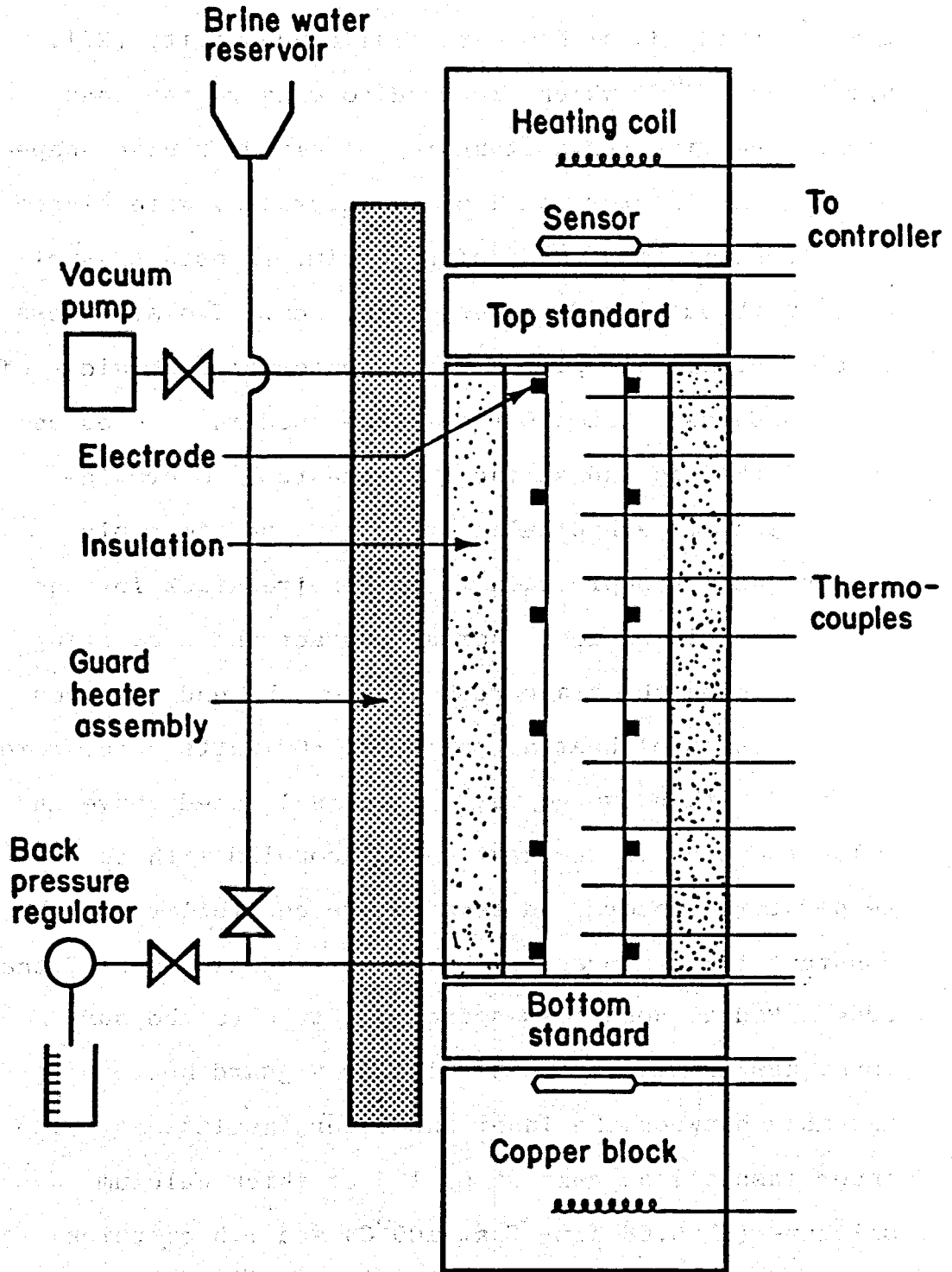
analysis for natural porous media systems based on their experimental results is limited. In order to make a comparison between analysis and experiment, the following experimental work was considered to be necessary.

### III.2. Experimental Apparatus

Figure 3.4 shows the configuration of the experimental apparatus. It consists of a 25 cm long, 5.08 cm I.D., 7 cm O.D., hollow cylindrical Lexane tube packed with unconsolidated Ottawa sand. The temperature distribution was measured at the center of the tube by chromel-alumel thermocouples and provisions for measuring saturation values were provided by electrical resistance measurements between pairs of silver-coated copper electrodes placed on the inner wall of the tube. Holes about 1.5 mm diameter were drilled through the wall of the Lexane tube for the passage of sheathed thermocouples and electrodes. A sealant\* was used to form a strong bond and seal the clearance between the inserted leads and the Lexane tube. In addition, a silicon rubber sealant was applied around the holes on the outer surface of the tubing. The flexibility of the silicon rubber sealant can stop possible leaks from the joints of two materials with different thermal expansion coefficients if the experimental process is carried over a large temperature range.

---

\*Eccobond 104, Emerson & Cuming, Inc.



XBL 818-3470

Figure 3.4 Schematic of one dimensional experimental apparatus.

The sand packed tube was mounted between two fired Lava\*\* standards of known thermal conductivity ( $2.11 \text{ W/m-}^\circ\text{C}$  at  $120^\circ\text{C}$ ) which are used to measure the heat flux. The fired Lava standards of circular disc shape,  $5.08 \text{ cm}$  in diameter and  $1.61 \text{ cm}$  thickness, were placed in concentric rings made of a polyimide resin (Vespel SP1)<sup>§</sup> with outside diameter of  $10.2 \text{ cm}$ . Two stainless steel thermocouple plates were mounted on both sides of the standards. Viton O rings were used in grooves on both of the two end surfaces of the tube to provide liquid seals. A hydraulic press was used to apply  $500 \text{ psi}$  axial compression to the entire stack for the purpose of giving good thermal contact and preventing leaks between the standards and the tube end surfaces.

Two sets of heating coils, of  $800 \text{ watts}$  each, were embedded within two copper cylinders located above and below the stack. The heaters are coupled with two temperature sensors and temperature controllers so that constant temperatures can be set at the two ends of the tube. Radial heat losses from the tube to the surroundings are minimized by placing a guard heater assembly between the inner and outer insulations. The inner insulations consist of  $1.5 \text{ cm}$  thick calcium silicate ( $\lambda = 0.06 \text{ W/m-}^\circ\text{C}$  at  $100^\circ\text{C}$ ) and  $1.5 \text{ cm}$  thick fiber glass ( $\lambda = 0.05 \text{ W/m-}^\circ\text{C}$ ). The outer insulation is  $2.5 \text{ cm}$  thick fiber glass. The Lexane tube itself is a

\*\* Natural Stone, Grade A, Aluminum Silicate, American Lava Corp.

§ Du Pont Company.

good insulator ( $\lambda = 0.17 \text{ W/m-}^\circ\text{C}$ ). The guard heater assembly has two heating coils wound on two ceramic semi-cylindrical sections with variable spacing and three small tape heaters. Each heater has its own Variac controller so that the guard temperature may be adjusted to fit the sand pack temperature profile closely.

The pore fluid pressure was controlled by a back-pressure regulator with the range of 0-6 psig, which was connected to the bottom inlet of the Lexane tube. A pressure transducer was used to measure the pressure difference between top and bottom end points of the sand pack. Stainless steel tubing 1/16" O.D. was used to connect the different components.

### III.3. Experimental Procedure

Two different grain-size Ottawa sands, 20-28 mesh and 65-100 mesh, were chosen for the porous media. In packing the tubes, a plastic ring was placed on top of the tube and 100 psi axial compression was applied to the system. The sand was slowly poured through an opening on the side of the plastic ring into the tube. As the sand was being added, a compressed-air driven vibrator was placed against the wall of the tube to vibrate the pack for effective packing. The usual plunger packing process was not used to avoid damaging or relocating the thermocouples inside the tube. After the packing was complete, the porosity was calculated as

$$\phi = 1 - \frac{\text{mass of sand packed}}{(\text{volume of empty tube})(\text{density of sand})}$$

After packing, the plastic ring was removed and replaced by the top standard holder. The system was again placed under 500 psi axial compression.

For liquid saturating the sand pack, a vacuum pump was attached to the top of the tubing, while the lower end of the tubing was connected to a vacuum gauge to measure the degree of vacuum. Unfortunately, there was difficulty in obtaining satisfactory vacuum even after ten hours of operation. (The degree of vacuum achieved was about 3 mm Hg.) This is probably due to minute leaks in the system and the small diameter of the outgassing tubing. With some vacuum in the system, deaerated brine (2000 ppm  $KCl$ ) was flowed into the sand pack through the lower tubing at a flow rate of about 10 cc/min. The valve on the top tubing was closed until the brine reached the top surface. The initial liquid saturation was calculated by measuring the net amount of water that flowed into the tube.

After saturating the sand pack, a permeability test was run by applying a constant water head between the two end surfaces of the tube. The absolute permeability was calculated by use of Darcy's law.

The test was started by setting the temperature controllers so that both ends of the tube reached the desired temperatures. The temperature at the hotter side was between  $122^{\circ}C$  and  $100^{\circ}C$ , and the temperature

at the colder side was specified between  $100^{\circ}\text{C}$  and the ambient temperature. Due to the density difference between vapor and water, some brine is displaced from the tube as the result of phase changes. The back pressure regulator setting was kept at a constant value slightly above atmospheric pressure. The amount of displaced brine was measured by a calibrated collection tube located at the outlet of the regulator. It usually took ten hours to achieve steady state conditions which could easily be observed by the continuous recording of temperatures. Each experiment ended when the steady state condition was reached. Sometimes the temperature controllers for both end surfaces were reset to start another experiment. After completion of the test, the sample was weighted to check the mass balance.

#### III.4. Experimental Results

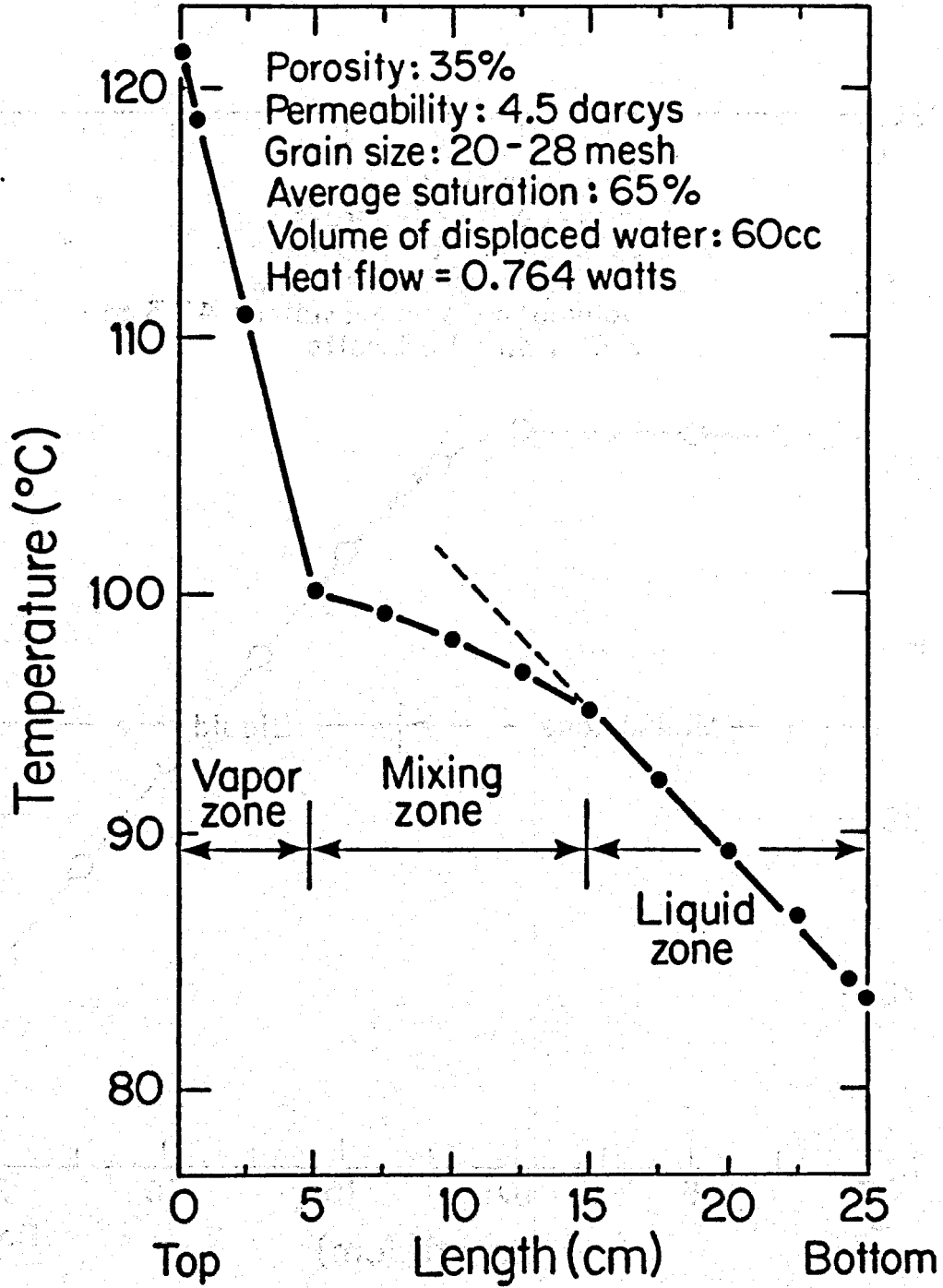
Generally speaking, the experiments were quite successful. The heat pipe phenomenon can be easily achieved and the experimental results were quite reproducible.

Fifteen experiments were carried out for the different temperature settings at the two end surfaces as shown in Table 3.1. Since similar results were obtained from the experiments, only four typical sets of experimental results are presented here. Two sand-grain sizes, 20-28 mesh and 65-100 mesh, were used. For Figs. 3.5 through 3.7, the hotter surface was on the



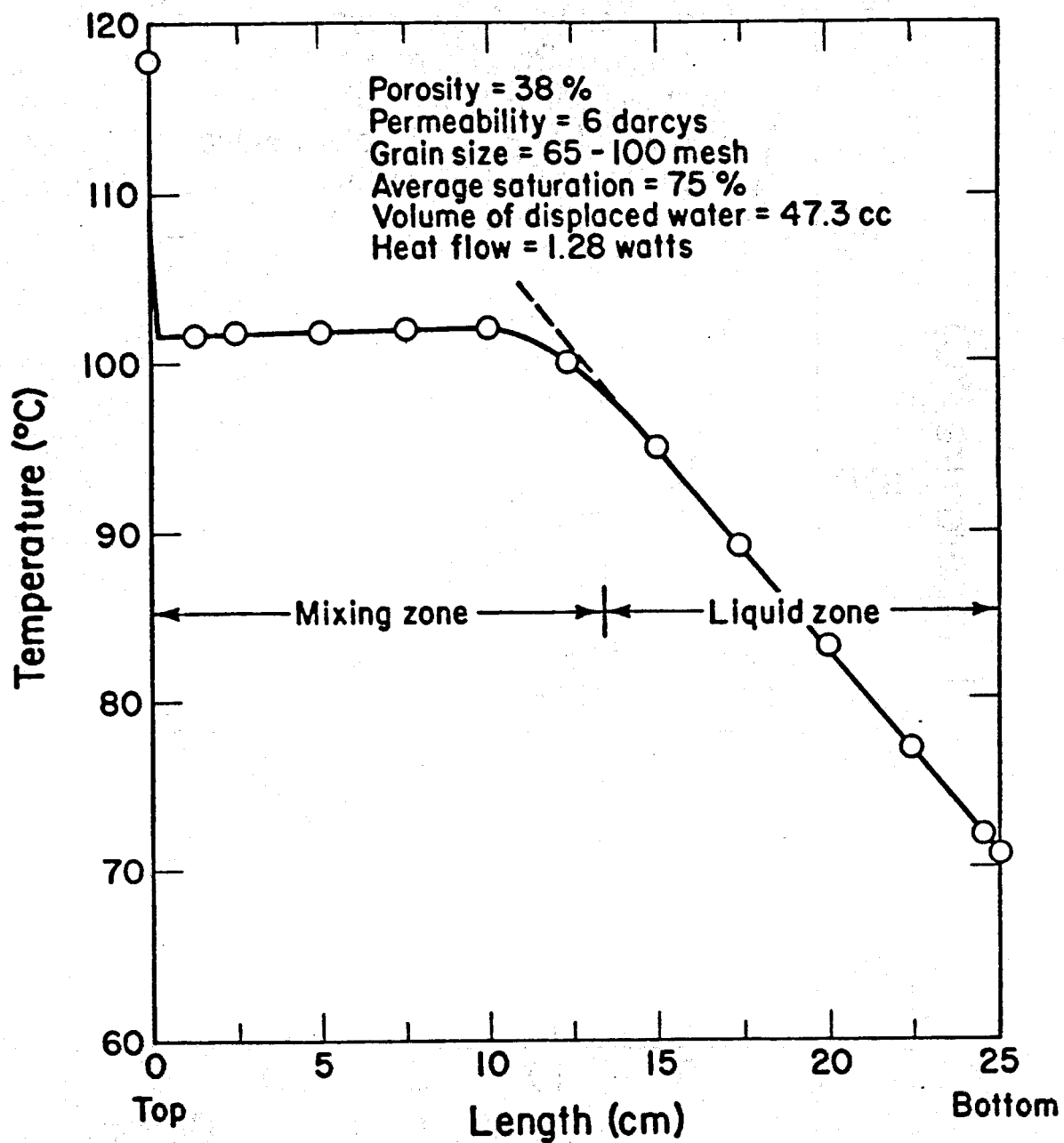
Table 3.1 List of experimental tests

Test No.	Date	Grain size (mesh)	Temperature settings at top-bottom surfaces (°C)
1	Mar. 15	20-28	92.8- 43.9
2	Mar. 15	20-28	105.7- 47.8
3	Mar. 16	20-28	115.7- 46.9
4	Mar. 16	20-28	113.3- 80.1
5	Mar. 23	20-28	74.3-107.6
6	May 15	20-28	119.7- 68.9
7	May 16	20-28	122.2- 84.1
8	Apr. 7	65-100	112.6- 58.2
9	Apr. 8	65-100	108.1- 60.4
10	Apr. 8	65-100	108.5- 87.4
11	Apr. 9	65-100	116.9- 61.4
12	Apr. 10	65-100	58.5-105.9
13	Apr. 30	65-100	89.6- 43.3
14	May 3	65-100	112.1- 86.7
15	Dec. 3	65-100	117.7- 70.6



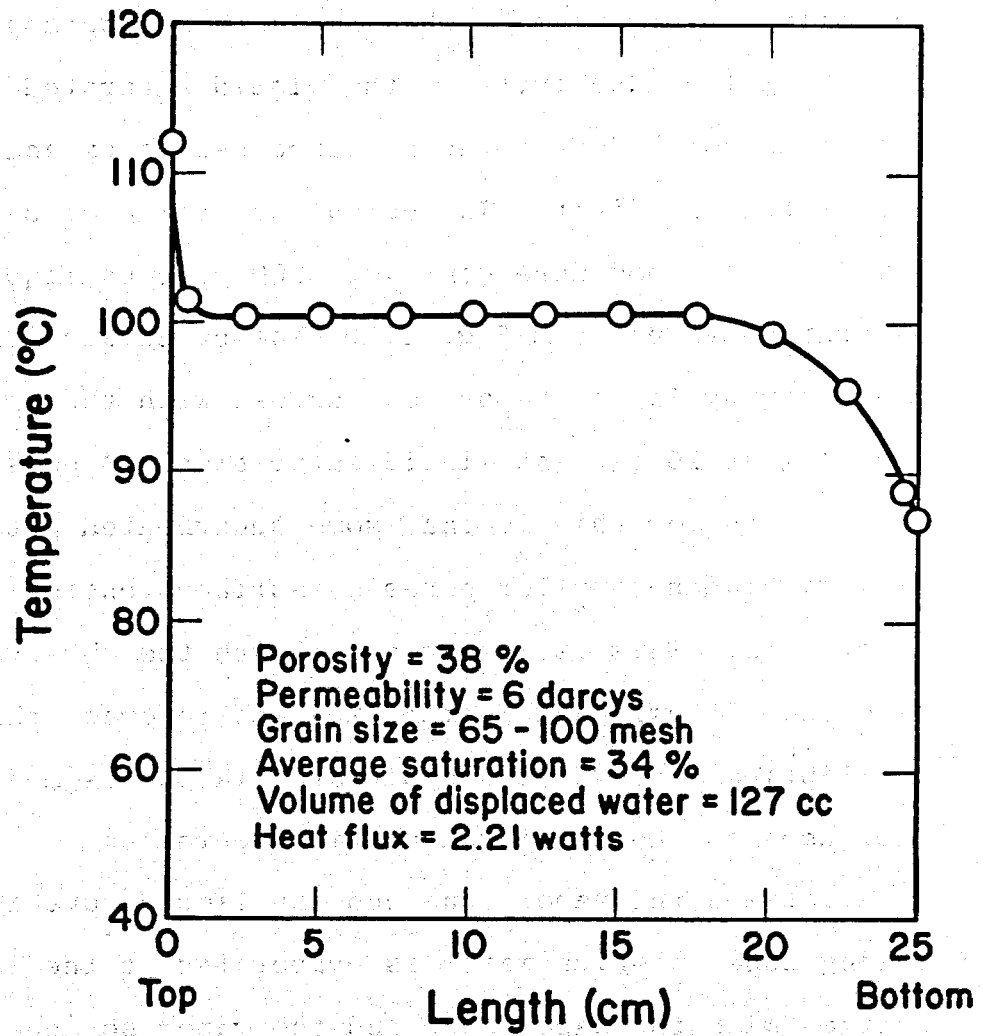
XBL 7910 - 4556

Figure 3.5 Temperature profile of Ottawa sand pack.



XBL 814-9111

Figure 3.6 Temperature profile of Ottawa sand pack



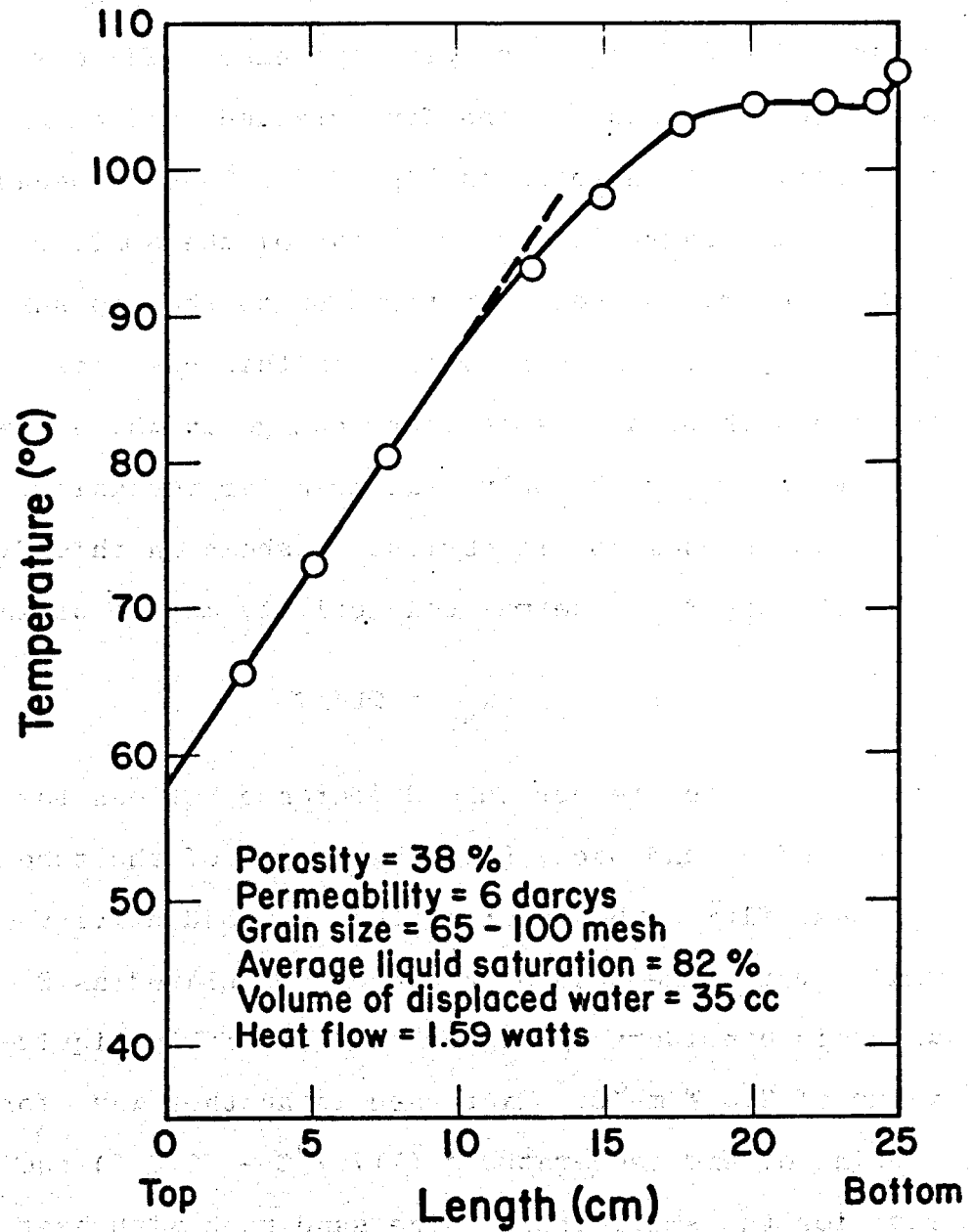
XBL 818-3469

Figure 3.7 Temperature profile of Ottawa sand pack

top end. For Fig. 3.8, the colder temperature was at the top of the tube.

Figure 3.5 shows the temperature profile for the large grain-size Ottawa sand sample. The two straight line portions of the profile imply that conduction is the only heat transfer mechanism in these two zones. The thermal conductivity of the liquid saturated zone can be calculated from the measured heat flux and the temperature gradient. The calculated value of 3.3 W/m-°C is in good agreement with 100 percent liquid saturation value from Fig. 1.1. The calculated thermal conductivity in the vapor zone agrees with the value in Fig. 1.1 at 10 percent liquid saturation. A possible explanation for this is that some superheated water is held within the smaller pores by surface tension and adsorption. This is in agreement with the observations of Calhoun, Lewis and Newman (20) who reported that the equilibrium vapor pressure of water in porous media decreases as the liquid saturation decreases.

Between the vapor zone and the liquid zone is the mixing zone in which water is evaporated at the intersection with the vapor zone and the vapor so generated is condensed within the mixing zone. The existence of vapor at a temperature below its boiling point is due to the presence of a small amount of air in the system. In all the experiments, the initial air saturation of the sand packs ranges from 2 percent to 15 percent even though the vacuum saturation procedure was applied.



XBL 818-3471

Figure 3.8 Temperature profile of Ottawa sand pack

Figure 3.6 shows the temperature profile of the smaller grain-size Ottawa sand sample. The results are quite different from the previous case. There was no separate vapor zone in the fine-grained sand pack as in the previous case shown in Fig. 3.5. This is because the larger capillary pressure gradient of the smaller grain-size sand brings the water right up to the top surface of the sand pack. The mixing zone in this case has a large portion without any temperature change in which the latent heat exchange is the only heat transfer mechanism. The heat pipe phenomenon is obvious as shown in this figure.

The apparent thermal conductivity may be defined as:

$$\lambda_{ap} = QL/\Delta T$$

where  $\Delta T$  is the temperature difference between the two end points of a sand pack,  $L$  is the length of the tube and  $Q$  is the heat flux. The apparent thermal conductivity of the small grain-size sand pack can be calculated as  $3.4 \text{ W/m}^\circ\text{C}$  which is considerably higher than its fully liquid-saturated value of  $2.6 \text{ W/m}^\circ\text{C}$ . Expressed in another way, for the same setting of end temperatures ( $117.7^\circ\text{C} - 70.6^\circ\text{C}$ ) the heat flux for the small grain size sand pack with heat pipe phenomenon was 1.28 watts compared to 0.97 watts for the fully liquid saturated sand pack.

Figure 3.7 shows the temperature profile for the smaller grain-size sand pack, but with different temperature settings at the two ends ( $110^\circ$  and  $86.5^\circ\text{C}$ ). The temperature readings indicate the presence of some

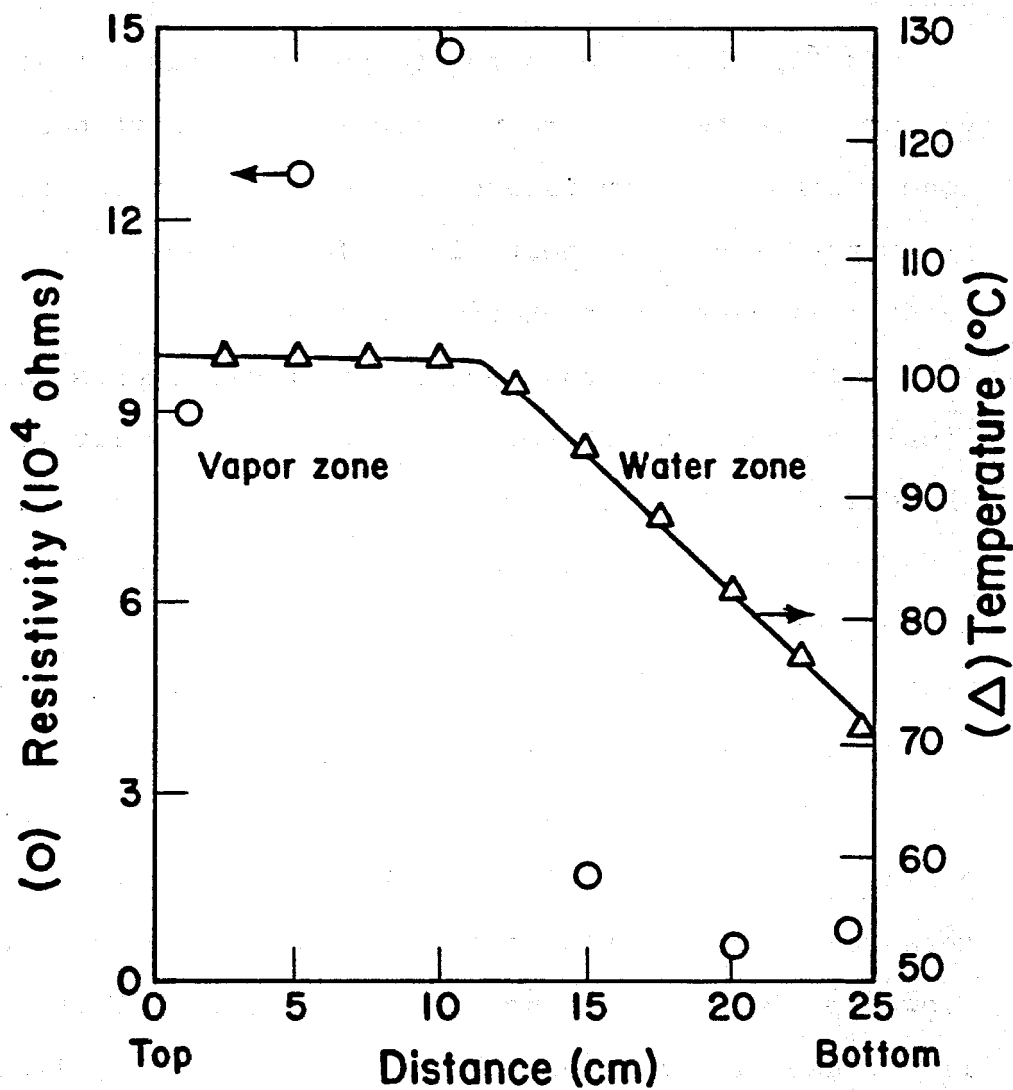
superheated steam in the top portion of the tube. This also means the irreducible water saturation was reached at the top surface. The heat pipe phenomenon exists over a greater length than the last test. The apparent conductivity increases to  $11.7 \text{ W/m-}^\circ\text{C}$  and the heat flux to 2.21 watts.

In Fig. 3.8, the hotter temperature was set at the bottom. The temperature profile shows a short heat pipe zone (without a temperature gradient). In this case, gravity enhances the heat pipe effect by assisting the water flow back to the hotter surface.

Unfortunately, the resistivity measurements for liquid saturation determination were only qualitatively successful. The resistivity readings in the mixing zone were erratic making it impossible to evaluate the local saturation values. However, the intersection between the liquid zone and the mixing zone was clearly indicated by a ten-fold or greater difference in the readings as shown in Fig. 3.9. Chen (21) made the following comments in his dissertation: "The resistivity method can be used to measure gas or oil saturation in gas-water or oil-water flow experiments by using conductive water. This method is not useful for boiling steam-water flow experiments. The main drawback is that the electrical conductivity of the liquid phase will change as the water starts to boil. Consequently, the change of liquid saturation will tend to be masked by changing water conductivity."



Porosity = 38 %  
 Permeability = 6 darcys  
 Grain size = 65 - 100 mesh  
 Average saturation = 75 %  
 Volume of displaced water = 47.3 cc  
 Heat flow = 1.28 watts



XBL 814-669

Figure 3.9 Example of resistivity measurement results.

### III.5. Comparisons of Theoretical Development with Experimental Results

The experimental results shown in Fig. 3.6 for the fine-grained sand pack were used to calculate the saturation profile from the numerical solution of Eq. (2.8) using the third-order Runge-Kutta method,

$$S_{i+1} = S_i + \frac{\Delta x}{6} (\alpha_1 + 4\alpha_2 + \alpha_3)$$

where  $S$  = liquid saturation

$\Delta x$  = grid size

$$\alpha_1 = f(S_i)$$

$$\alpha_2 = f\left(S_i + \frac{\Delta x}{2} \alpha_1\right)$$

$$\alpha_3 = f\left(S_i + 2\Delta x \alpha_2 - \Delta x \alpha_1\right)$$

$$f = \left[ \frac{\hat{m}_v}{K} \left( \frac{v_w}{k_w} + \frac{v_v}{k_v} \right) + \hat{g}(\rho_w - \rho_v) \right] \cdot \frac{1}{\left( -\frac{dP}{dS} \right)}$$

The mass flux  $m$  was obtained from  $m = Q/h_{fg}$ . The relative permeability values  $k_v, k_w$  were calculated from the Corey equation (22) as follows:

$$k_v = (1-\beta)^2(1-\beta^2) \quad (3.1)$$

$$k_w = \beta^4 \quad (3.2)$$

$$\beta = \frac{S - S_{ig} - S_{iw}}{1 - S_{ig} - S_{iw}} \quad (3.3)$$

where  $S_{ig}, S_{iw}$  are irreducible gas and water saturations, respectively. The capillary pressure versus saturation curve was obtained by experimental measurement (centrifugal method) and was represented by the following regressional formula:

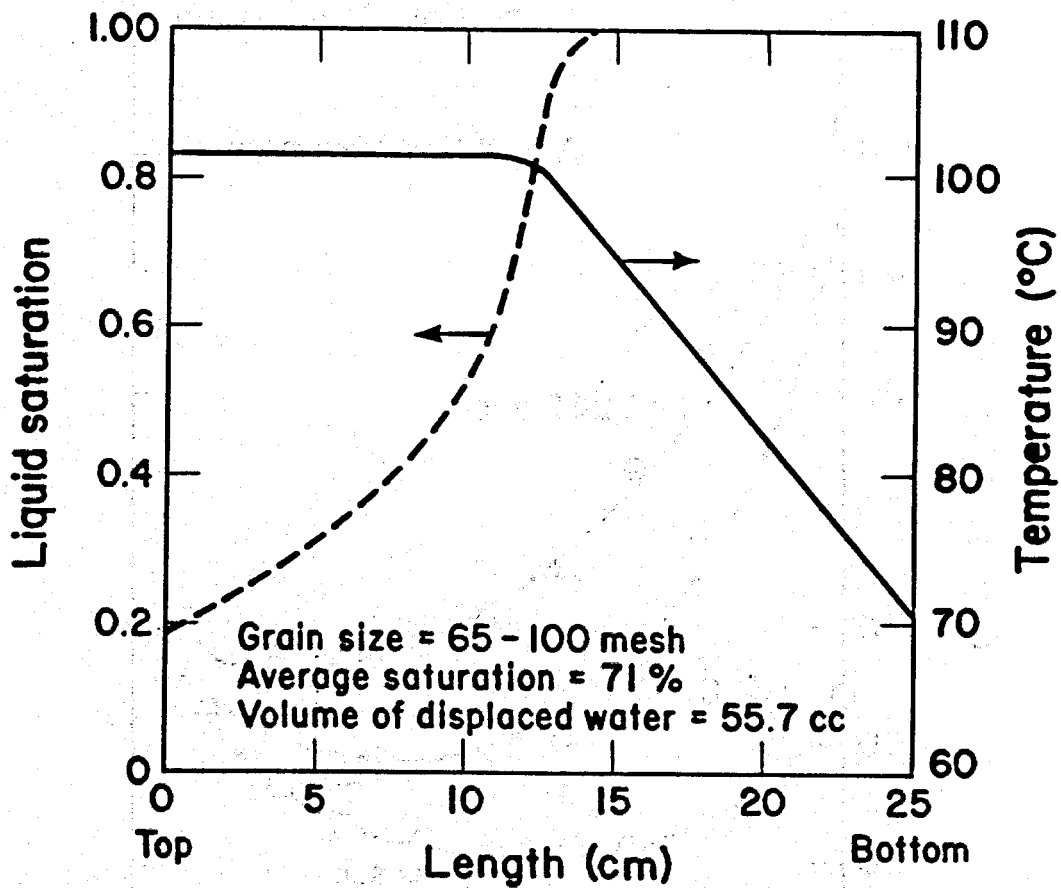
$$P_c = (72.7 - 607.3 \times S_w + 2494.6 \times S_w^2 - 5556 \times S_w^3 + 6842 \times S_w^4 - 4359 \times S_w^5 + 1111.1 \times S_w^6) / 1033.6$$

where  $P_c$  is in atm. Note that the above formula was obtained from an air-water system. Details of this centrifugal method of determining  $P_c$  are clearly described by Castor (23).

Based on the above measurement, the irreducible water and gas saturations were assumed to be 10 percent and 4 percent respectively, then the Runge-Kutta results were obtained as shown in Fig. 3.10. The volume of water displaced in this experiment was 47.3 cc compared with a calculated value of 55.7 cc. This difference is probably due to the use of sand property data from an air-water system since data for a steam-water system were not available. Chen, Council and Ramey (15) have reported a difference in relative permeability curves between an air-water system and a steam-water system. The capillary pressure data obtained from experiment is also for an air-water system.

Another way to compare the experimental results with theory is to run the two-phase computer program described in Chapter IV for the same initial and boundary conditions. Figure 3.11 shows comparisons between numerical results and experimental data at different time steps. The final steady state result is shown in Fig. 3.12.

All the comparisons show good agreement between experimental results and the theoretical development and also



XBL 814-9110A

Figure 3.10 Calculated saturation profile.

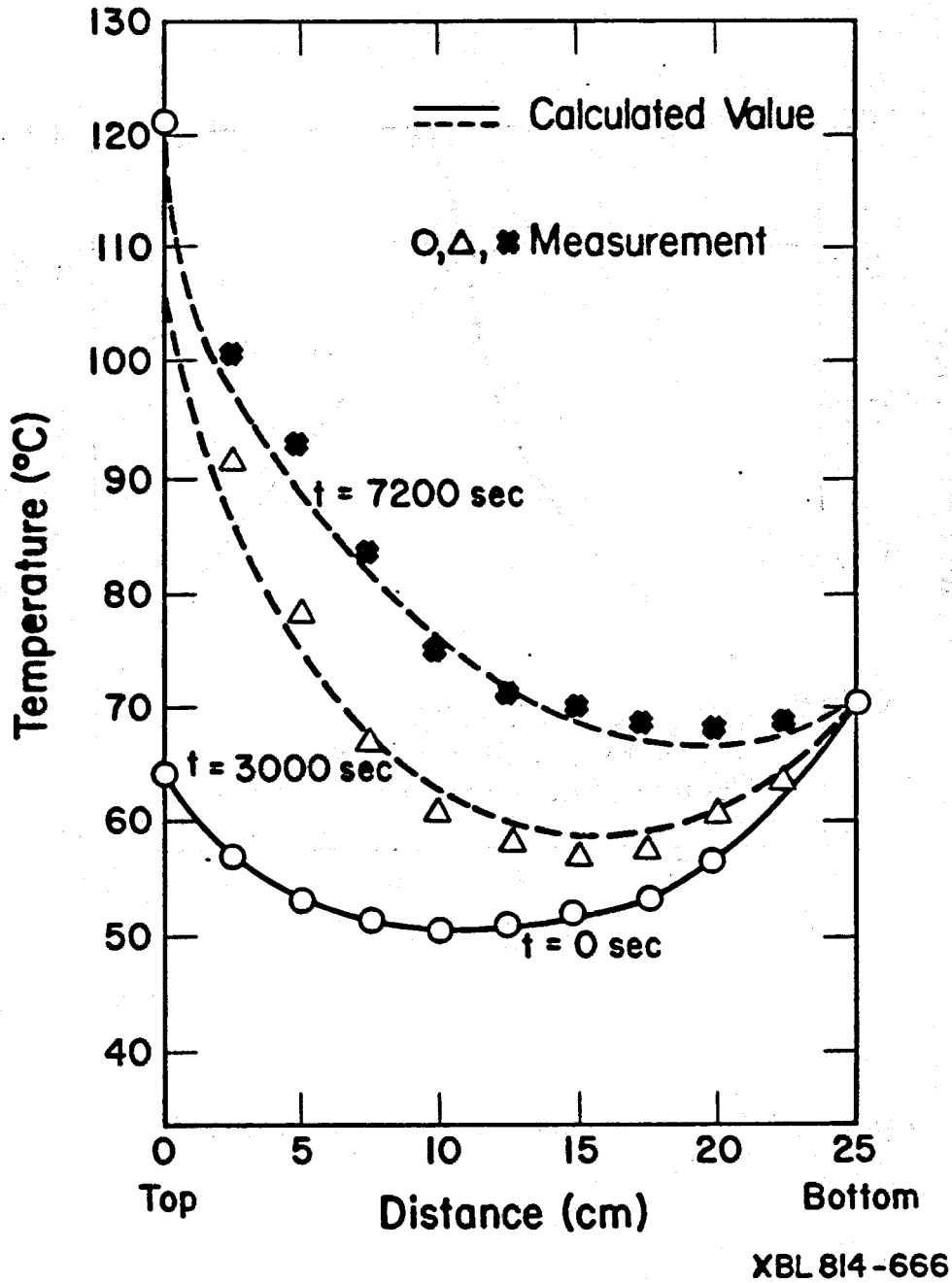
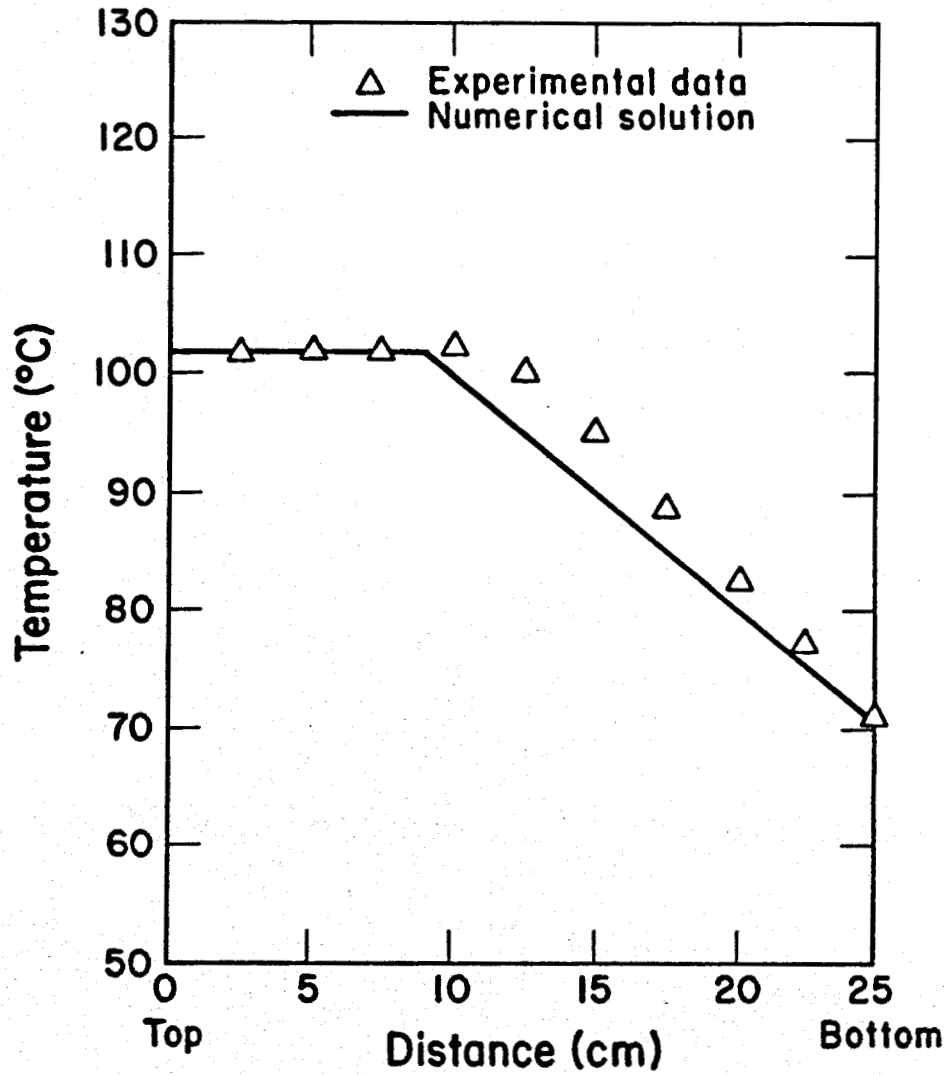


Figure 3.11 Temperature profiles at different time steps—experimental and calculated.



XBL 818-3475

Figure 3.12 Steady state temperature profile of numerical results compared with experimental data

demonstrate the validity of the two-phase computer program developed later in this work. Presence of the heat pipe phenomenon in a long sand packed tube is confirmed through the experiment. The assumption that there is a very small temperature gradient in the heat pipe zone is confirmed by the temperature readings.

## CHAPTER IV. NUMERICAL SIMULATION OF WELLBORE HEAT LOSSES

### IV.1. Introduction

In the case of steam injection or geothermal production, there is transfer of heat between the fluid inside the wellbore and the surrounding formation due to the temperature difference between the fluid and the formation. Several authors (24,25,26) have presented mathematical models, but all of them consider only heat conduction to calculate heat losses from the wellbore into the formation.

At depths not too far from the surface, the temperature around the wellbore can exceed the boiling temperature of pore fluids depending on the local formation pressure. Under these conditions, the heat pipe phenomenon described in Chapter III may occur in the formation surrounding the wellbore. The heat losses from the wellbore may increase several times over that for the case without phase changes. In order to study this two-phase problem, a geothermal reservoir simulator needs to be developed.

As mentioned in the literature on geothermal reservoir simulation, the major difficulty is the simulation of blocks where changes from one phase to the other occur. Recently, many authors have achieved stable solutions but without the provision of changing states. Sutter (27) employed a staged calculation in one-dimensional steamflood simulation. The pressures and saturations were calculated simultaneously



from mass balances using Newtonian iteration on nonlinearities occurring in the accumulation terms. The energy equation is solved separately by non-iterative application of the ADI procedure. The mass balance and energy balance equations were coupled by virtue of the condensation term, which can be estimated in a specially derived manner for use in solution of the mass balances. In general, Sutter avoided the excessive computer time of completely simultaneous solutions at the expense of a small error.

Mercer and Faust (28) developed a two-dimensional (areal) two-phase geothermal model using a so-called Galerkin finite element formulation in space and finite difference formulation for time. They chose pressure and enthalpy as dependent variables and solved for these two variables simultaneously.

Garg et al. (29) transformed the fundamental equations of mass and energy balances into four equations for four unknowns, mixture (liquid-vapor) density, mixture internal energy, rock internal energy and mass transfer rate from liquid to vapor due to phase change. They set some constitutive relations to make the above transformation. The iterative ADI method was employed to solve the four unknowns simultaneously.

Lasseter et al. (30) used the finite element method to develop a computer program called SHAFT for multi-phase multi-dimensional simulation of geothermal reservoirs. Solutions were obtained by solving for two unknowns,

density and internal energy of the fluid mixture (liquid-vapor), as functions of time and position within the system. In their approach, one starts with the initial energy distribution and assumes that this distribution remains constant over the time step, then the density distribution is solved. With this new density distribution, the energy solution is then obtained. This process is continued until the differences between successive estimates of the energy and density distributions are within acceptable limits. Capillary pressure is ignored in their program.

Atkinson (31) transformed the flow and energy equations into a different form so that the dependent variables became pressure and liquid saturation. The Crank-Nicholson implicit scheme was used with the Newton-Raphson iteration for these non-linear equations. His work is restricted to the one-dimensional problem and capillary pressure is neglected.

Faust and Mercer (32) compared the finite difference and the finite element models, and found that the latter is more suitable for hot-water reservoirs due to less numerical diffusion and better approximations of boundary and internal geometries (with fewer node points). For vapor-dominated systems, the finite-difference model appears superior because it reduces mass and energy balance errors and exhibits less numerical oscillation.

Although all of the above authors claimed stable and accurate solutions, the work of some authors (31,32)

suffered numerical difficulties for the initial fully liquid saturated condition. The problem of changing from sub-cooled liquid to saturated steam was avoided by starting the simulation at reduced initial pressure so that saturated conditions would be present.

Coats et al. (33) presented a new technique for numerical simulation of the steamflood process to solve mass balance and energy balance equations simultaneously. Thomas and Pierson (34) extended the method to a geothermal system. The mathematical model developed in the present dissertation is similar to their formulation, but differs from theirs in the following aspects.

1. The capillary pressure is included in the calculation of pressure distribution.
2. The vapor pressure lowering effect is considered.
3. The transmissibilities and densities for both phases are treated implicitly.

#### IV.2. Mathematical Modeling

The governing equations for two phase flow in porous media are:

mass conservation for water phase:

$$\nabla \cdot \left[ \frac{Kk_w}{v_w} (\nabla P_w - \rho_w \hat{g}) \right] + Q_c = \phi \frac{\partial}{\partial t} (\rho_w S_w) \quad (4.1)$$

mass conservation for vapor phase:

$$\nabla \cdot \left[ \frac{Kk_v}{v_v} (\nabla P_v - \rho_v \hat{g}) \right] - Q_c = \phi \frac{\partial}{\partial t} (\rho_v S_v) \quad (4.2)$$

and energy conservation:

$$\begin{aligned} \nabla \cdot \left[ h_w \frac{Kk_w}{v_w} (\nabla P_w - \rho_w \hat{g}) \right] + \nabla \cdot \left[ h_v \frac{Kk_v}{v_v} (\nabla P_v - \rho_v \hat{g}) \right] + \nabla \cdot (\lambda \nabla T) \\ = \phi \frac{\partial}{\partial t} (\rho_w S_w U_w) + \phi \frac{\partial}{\partial t} (\rho_v S_v U_v) + (1-\phi)(\rho C_p)_{\text{rock}} \frac{\partial T}{\partial t} \end{aligned} \quad (4.3)$$

where  $Q_c$  is condensation rate, and  $h$  and  $U$  are enthalpy and internal energy, respectively.

Besides the above three equations, the thermodynamic equilibrium relationship between pressure and temperature for steam must be satisfied. The above equations are coupled to each other, therefore they may be solved simultaneously. The computing time would be very large if the four variables  $T$ ,  $P_w$ ,  $P_v$  and  $S_w$  appeared in a same matrix form of the finite difference equations. However, the following mathematical manipulations can be made in order to establish an efficient numerical scheme.

The condensation term  $Q_c$  in Eq. (4.1) and the evaporation term  $-Q_c$  in Eq. (4.2) can be eliminated by adding the two equations

$$\begin{aligned} \nabla \cdot \left[ \frac{Kk_w}{v_w} (\nabla P_w - \rho_w \hat{g}) \right] + \nabla \cdot \left[ \frac{Kk_v}{v_v} (\nabla P_v - \rho_v \hat{g}) \right] \\ = \phi \frac{\partial}{\partial t} (\rho_w S_w + \rho_v S_v) \end{aligned} \quad (4.4)$$

For further simplification, the following new variables are defined:

$$\delta P = P_V^{n+1} - P_V^n,$$

$$\delta T = T^{n+1} - T^n,$$

$$\delta S_w = S_w^{n+1} - S_w^n$$

where  $n+1$  and  $n$  denote present and previous time steps, respectively. Then Eq. (4.3) and Eq. (4.4) can be rearranged as follows:

$$\nabla \cdot [(\tau_w + \tau_v) \nabla \delta P] = C_{11} \delta S_w + C_{12} \delta T + C_{13} \delta P - R_1 \quad (4.5)$$

$$\nabla \cdot [(\tau_H) \nabla \delta P] = C_{21} \delta S_w + C_{22} \delta T + C_{23} \delta P - R_2 \quad (4.6)$$

where  $\tau_w = \frac{Kk_w}{v_w}$ , flow transmissivity for water

$\tau_v = \frac{Kk_v}{v_v}$ , flow transmissivity for vapor

$$C_{11} = \phi(\rho_w^{n+1} - \rho_v^{n+1})/\Delta t$$

$$C_{12} = 0$$

$$C_{13} = \phi(S_v^n \frac{\partial \rho_v}{\partial P_v})/\Delta t$$

$$R_1 = -\nabla[\tau_w(\nabla P_w^n - P_c^{n+1} + P_c^n - \rho_w \hat{g})] - \nabla \cdot [\tau_v(\nabla P_v^n - \rho_v \hat{g})]$$

$\tau_H = h_w \tau_w + h_v \tau_v$ , thermal transmissivity

$$C_{21} = \phi(\rho_w U_w^{n+1} - \rho_v U_v^{n+1})/\Delta t$$

$$C_{22} = \phi(\rho_w S_w^n \frac{\partial U_w}{\partial T} + \rho_v S_v^n \frac{\partial U_v}{\partial T})/\Delta t$$

$$C_{23} = \phi(U_v^{n+1} S_v^{n+1} \frac{\partial \rho_v}{\partial P_v})/\Delta t$$

$$R_2 = -\nabla[h_w \tau_w(\nabla P_w^n - \nabla(P_c^{n+1} - P_c^n) - \rho_w \hat{g})] \\ - \nabla[h_v \tau_v(\nabla P_v^n - \rho_v \hat{g})] - \nabla \cdot \lambda \nabla T^n$$

The above relations are derived in detail in Appendix A.

One more equation needs to be incorporated with Eq. (4.5) and Eq. (4.6) for solving the three new defined variables,  $\delta P$ ,  $\delta S$  and  $\delta T$ . This can come from the thermodynamic equilibrium or phase relationship

$$0 = C_{31}\delta S_w + C_{32}\delta T + C_{33}\delta P + R_3 \quad (4.7)$$

The coefficients and residual in Eq. (4.7) depend on the state of a block at time  $n+1$ . For example, if saturated steam is present at time step  $n+1$ , then

$$\begin{aligned} \delta P &= P_{\text{sat}}(T^{n+1}) - p^n \\ &= P_{\text{sat}}(T^n) + \frac{P_{\text{sat}}(T^{n+1}) - P_{\text{sat}}(T^n)}{T^{n+1} - T^n} \delta T - p^n \\ &= P_{\text{sat}}(T^n) + \left(\frac{dP_{\text{sat}}}{dT}\right) \delta T - p^n \end{aligned}$$

therefore, for the case

$$C_{31} = 0$$

$$C_{32} = -\left(\frac{dP_{\text{sat}}}{dT}\right)$$

$$C_{33} = 1$$

$$R_3 = p^n - P_{\text{sat}}(T^n)$$

If subcooled liquid is present at time  $n+1$ , then  $\delta S_w = 1 - S_w$

$$C_{31} = 1$$

$$C_{32} = 0$$

$$C_{33} = 0$$

$$R_3 = S_w^n - 1$$

When the liquid saturation is below the irreducible water saturation, the thermodynamic equilibrium relationship between temperature and pressure has to be modified to the following form due to the vapor pressure lowering effect (20)

$$P_v = P_o e^{-CS_w^{-4}}$$

where  $P_o$  is the saturation pressure for the case of flat surface between water and vapor, and  $C$  is a constant equal to  $5.2 \times 10^{-7}$ . This modified formula was suggested by Moench and Herkerlrath (35). As a consequence of the above, Eq. (4.7) becomes

$$P_o e^{-CS_w^{-4}} (4CS_w^{-5}) \delta S_w + \left( \frac{\partial P_o}{\partial T} \right)_{\text{sat}} e^{-CS_w^{-4}} \delta T - \delta P = 0$$

since

$$\delta P = \frac{\partial P}{\partial S_w} \delta S_w + \frac{\partial P}{\partial T} \delta T$$

Furthermore, the variables  $\delta T$ ,  $\delta S_w$  can be eliminated by operating on Eq. (4.5), Eq. (4.6) and Eq. (4.7), then a single partial differential equation with one unknown  $\delta P$  is obtained as follows

$$A_1 [\nabla(\tau_w + \tau_v) \nabla \delta P] - A_2 \nabla[\tau_H \nabla \delta P] = A_3 \delta P + A_4 \quad (4.8)$$

$$\text{where } A_1 = C_{21} [C_{32} C_{11} - C_{11} C_{31}] - C_{31} [C_{22} C_{11} - C_{12} C_{21}]$$

$$A_2 = C_{11} [C_{32} C_{11} - C_{12} C_{31}]$$

$$A_3 = [C_{33} C_{11} - C_{13} C_{31}] \cdot [C_{22} C_{11} - C_{12} C_{21}]$$

$$- [C_{23} C_{11} - C_{13} C_{21}] \cdot [C_{32} C_{11} - C_{12} C_{31}]$$

$$A_4 = [C_{11} R_3 - R_1 C_{31}] [C_{22} C_{11} - C_{12} C_{21}]$$

$$- [R_2 C_{11} - R_1 C_{21}] [C_{32} C_{11} - C_{12} C_{31}]$$

The details of this derivation are shown in Appendix A.

Equation (4.8) is an elliptic type partial differential equation and can be solved implicitly. The Gaussian elimination method is employed here to solve the finite difference equations.

After the  $\delta P$  solution is obtained, the  $\delta T$  and  $\delta S_w$  solutions can be solved explicitly by the following equations:

$$\delta T = \{C_{31} \nabla[\tau_H \nabla \delta P] - [C_{31} C_{23} - C_{21} C_{33}] \delta P - (R_2 C_{31} - R_3 C_{21})\} / [C_{22} C_{31} - C_{21} C_{32}] \quad (4.9)$$

$$\delta S_w = \{\nabla \cdot (\tau_w + \tau_v) \delta P - C_{12} \delta T - C_{13} \delta P - R_1\} / C_{11} \quad (4.10)$$

Since the above equations are highly non-linear, the iteration process is repeated until a convergence criterion can be met. Generally speaking, this is a very efficient geothermal reservoir simulator. Instead of solving a set of coupled partial differential equations, only a single



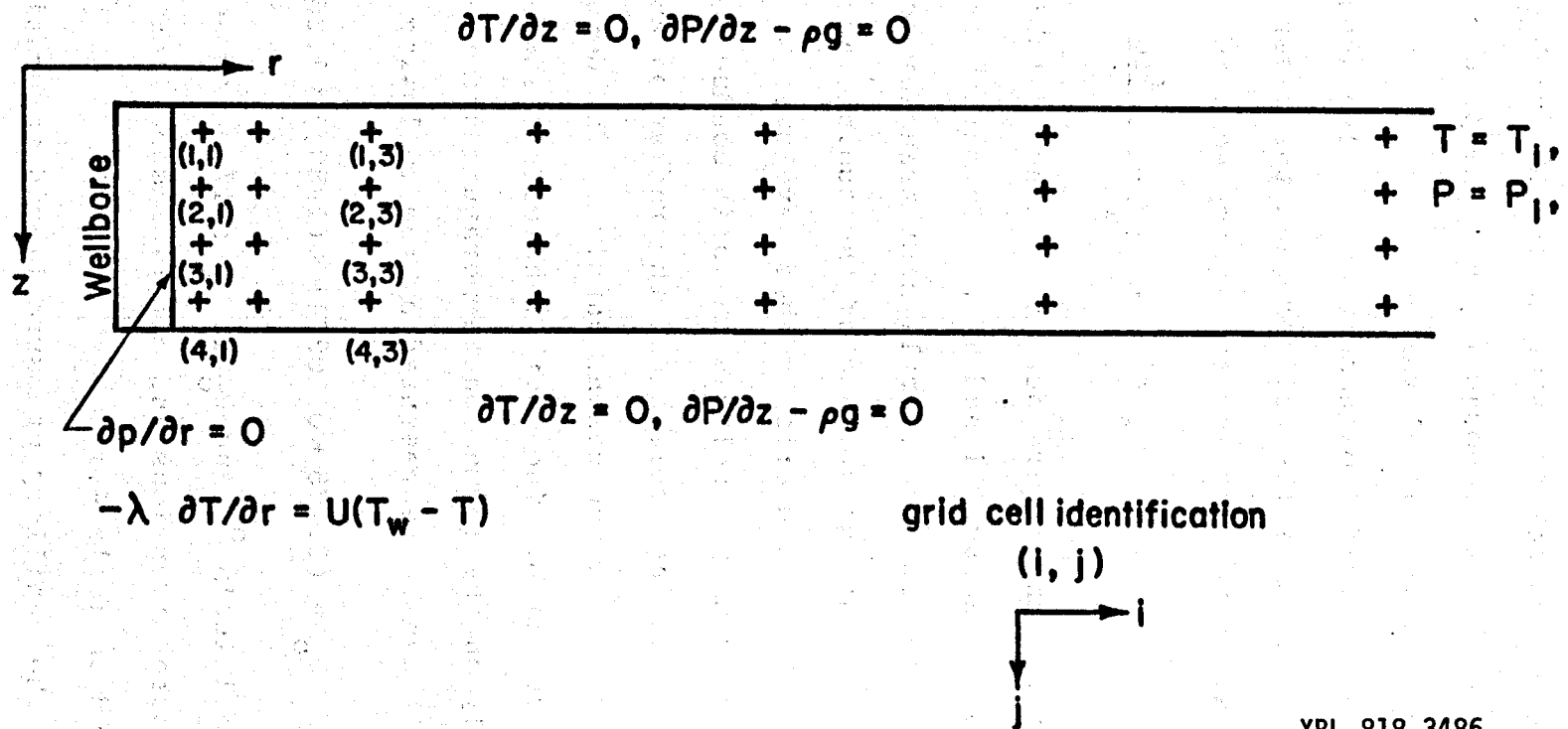
pressure equation is implicitly solved. Besides the advantage of saving computing time, this simulator always satisfies the thermodynamic equilibrium condition between water and steam and the mass conservation law. It also takes into account the vapor pressure lowering effect below irreducible water saturation and the capillary pressure effect.

#### IV.3. Numerical Formulation for Wellbore System

Figure 4.1 shows the configuration of the wellbore surroundings. A  $4 \times 7$  grid system is used, the distance between two successive grid points in the vertical direction being 30.5 cm. The distances from the wellbore intersection to each grid point in the horizontal direction are 15.25 cm, 45.75 cm, 106.75 cm, 198.25 cm, 320.25 cm, 472.75 cm, 655.75 cm. Theoretically, a semi-infinite region should be used for calculating the radial heat losses from a wellbore. Under the limitation of a computer account budget, the above grid system was chosen. As observed from the numerical results in the calculation of temperature and saturation, the influence of the wellbore does not reach the second farthest grid point. The pressure does change at points beyond to allow water flow inward or outward.

The upper and lower boundaries are two impermeable layers, so the pressure boundary conditions can be specified as:

$$\frac{\partial P}{\partial z} - \rho \hat{g} = 0$$



XBL 818-3486

Figure 4.1 Configuration of the wellbore surrounding.

It is also assumed that heat transfer is negligible at these boundaries for simplifying the problem.

At the outer boundary, all the properties are assumed to keep their initial values.

A no fluid flow condition is also assumed at the intersection of the wellbore and the reservoir. The boundary condition for the energy equation is

$$-\lambda \frac{\partial T}{\partial r} = U_o (T_w - T) \cdot \frac{r_{to}}{r_h}$$

where  $r_{to}$  and  $r_h$  are outside radius of tubing and the wellbore radius.  $T$  and  $T_w$  are formation and wellbore temperatures. The overall heat transfer coefficient  $U_o$  based on outside surface of the tubing, was calculated from a trial and error method developed by Willhite (26). The calculation includes the heat conduction through the tubing, casing, cement and the radiation and natural convection in the casing annulus. The details are given in Appendix B. The heat transfer coefficient depends weakly on the formation temperature and the calculated result can be represented by the following equation:

$$U_o = (3.475 + 0.002641 \times (T-80)) \times 1.354 \times 10^{-4}$$

where  $T$  is in  $^{\circ}\text{C}$  and  $U_o$  is in  $\text{cal/sec-cm sq-}^{\circ}\text{C}$ . The wellbore dimensions and material specifications are listed on Table 4.1.

The capillary pressure-liquid saturation relationship used in the analysis is adapted from Bruce and Welge (41). By using a curve-fitting technique, it can

Table 4.1 Specifications for overall heat transfer coefficient calculation (18)

Hole size (diameter)	24.5 cm
Casing:	
O.D.	17.8 cm
I.D.	15.9 cm
Tubing:	
O.D.	7.3 cm
I.D.	6.2 cm
Cement thermal conductivity	$2.1 \times 10^{-3}$ cal/sec-cm-C
Emissivity of outside tubing surface	0.9
Emissivity of inside casing surface	0.9
Injection steam temperature	315.6°C

be expressed as

$$P_c = 2.32 - 17.64 \times S_w + 53.2 \times S_w^2 - 78.6 \times S_w^3 + 56.9 \times S_w^4 - 16.16 \times S_w^5$$

where  $P_c$  is in atm. The relative permeabilities are calculated from Corey's equations (Eqs. (3.1)-(3.3)).

The other properties used in this simulation are listed in Table 4.2. Thermal conductivity of partially liquid saturated porous media can be calculated by the following equation (36):

$$\lambda = \lambda_d + (\lambda_w - \lambda_d) \sqrt{S_w}$$

where subscripts d and w denote the dry and the fully liquid saturated conditions, respectively. Some of the fluid properties depend on temperature and pressure, and can be expressed as follows (37):

viscosity of vapor (T in °C, and  $\mu_g$  in cp)

$$\mu_g = 0.879 \times 10^{-2} + 0.374 \times 10^{-4} T + 0.2 \times 10^{-8} T^2$$

Range: 100°C ~ 250°C

viscosity of water (T in °F,  $\mu_w$  in cp)

$$\mu_w = 2.185 / (0.04012T + 5.155 \times 10^{-6} T^2 - 1)$$

enthalpy of vapor (P in psi, h in Btu/lbm)

$$h_g = 1119 P^{0.01267}$$

Table 4.2 Input specifications for 2-D simulation

Porosity	0.2
Absolute permeability	0.1 darcys
Specific heat for water	1.0 cal/gm-°C
( $\rho C_p$ ) <sub>rock</sub>	0.47 cal/gm-°C
Thermal conductivity of formation:	
wet (100% liquid saturation)	$5.78 \times 10^{-3}$ cal/sec-cm-°C
dry (0% liquid saturation)	$1.24 \times 10^{-3}$ cal/sec-cm-°C
Initial temperature	26.6°C
Initial pressure	2.475 atm at upper boundary
	(15.25 meters hydrostatic pressure)
Irreducible water saturation	0.28
Irreducible gas saturation	0.05

density of vapor (P in psi,  $\rho$  in gm/cc)

$$\rho_g = 4.378 \times 10^{-5} P^{0.9588}$$

internal energy of vapor (T in  $^{\circ}\text{F}$ , U in Btu/lbm)

$$U_v = 995.3 + 0.4862T - 0.4618 \times 10^{-3} T^2$$

Range:  $193^{\circ}\text{F} \sim 400^{\circ}\text{F}$

internal energy of water (T in  $^{\circ}\text{F}$ , U in Btu/lbm)

$$U_w = -24.86 + 0.9313T + 0.1648 \times 10^{-3} T^2$$

Range:  $80^{\circ}\text{F} \sim 400^{\circ}\text{F}$

specific heat of vapor (T in  $^{\circ}\text{F}$ , U in Btu/lbm)

$$C_v = 0.4862 - 0.9236 \times 10^{-3} T$$

The central difference scheme is used to solve the partial differential equation. For example,

$$\frac{\partial}{\partial z} \left( a \frac{\partial T}{\partial z} \right) = \frac{a_{j+\frac{1}{2}}(T_{j+1} - T_j) - a_{j-\frac{1}{2}}(T_j - T_{j-1})}{(\Delta z)^2}$$

Since most of the coefficients are strong functions of the dependent variables, they are evaluated with updated values in the iteration procedure. The interblock coefficients are calculated by a weighting technique

$$a_{j+\frac{1}{2}} = a_j w + a_{j+1} (1-w)$$

If the coefficient is temperature or pressure dependent,  $w=0.5$  is adapted. If the coefficient is a function of liquid saturation, then 80 percent weighting factor is put

on the upstream point from where the flowing fluids come. Aziz (38), Lasseter and Witherspoon (39), and Blair, et al. (40) have reported that some sort of upstream weighting would probably give better results. The numerical results are very sensitive to the saturation dependent coefficients. An improper weighting factor could cause unstable or unreasonable results.

The convergence test can be satisfied if

$$|(Y^{K+1} - Y^K)|/Y^{K+1} < 0.01$$

where  $Y$  is any dependent variable and  $K$  denotes iteration steps. An automatic time step control is employed to save computing time. When any one of the saturation changes exceed a specified upper limit, the time step interval will be divided by two. Otherwise, the time interval is increased 20 percent for the next time step. There is also a maximum bounds for the time step interval.

#### IV.4. Verification of Numerical Model

It is necessary to compare the numerical results with either analytical or experimental results in order to confirm the validity of the numerical model. Unfortunately, neither the analytical solution nor an experiment for two-dimensional two-phase flow in porous media are available. However, there was a one-dimensional two-phase flow experiment conducted at Stanford University (42). The experimental apparatus was built around a Hassler-type core holder located in a constant temperature bath and was equipped

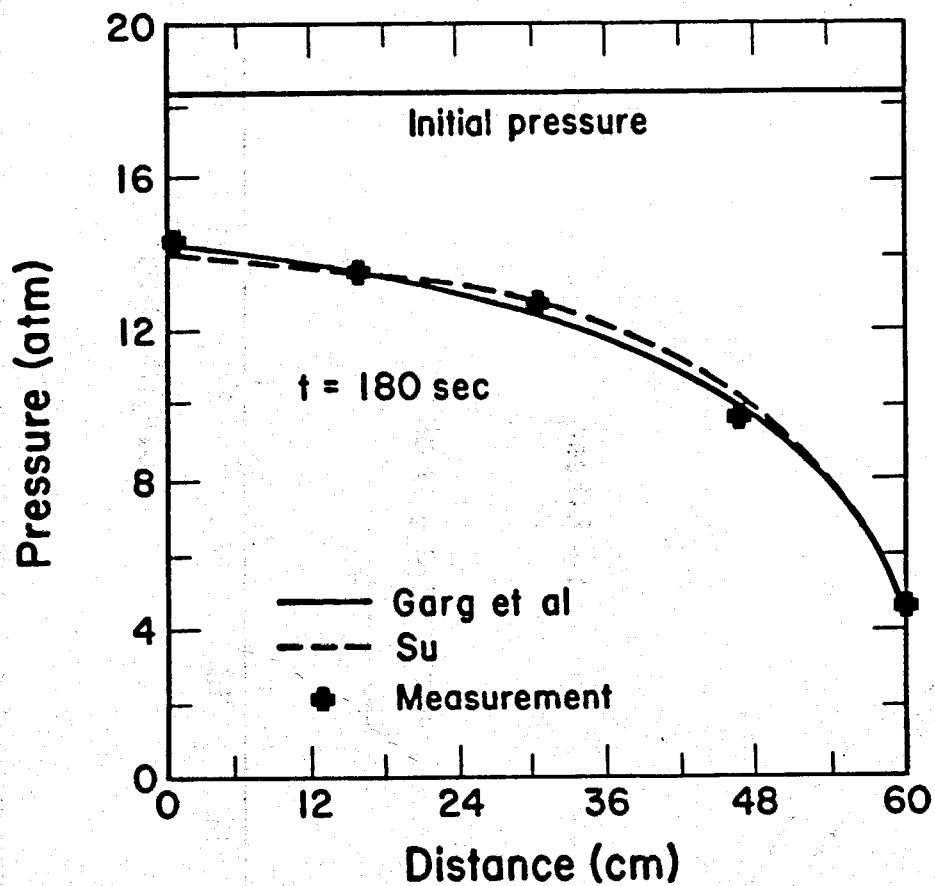


with five pressure taps and six temperature probes. The core has 60 cm in length, 5.1 cm in diameter, and was made of a synthetic consolidated sandstone (80 percent sand, 20 percent cement). Initially, the core was fully saturated with water at 18.16 atm, with temperature varying from 192.2°C at the left end to 182.8°C at the right end. Flow was initiated at the right end by opening a valve, and then the pressure at that end was dropped at a controlled rate.

For comparison with the above experimental results, the two-dimensional program was simplified into a one-dimensional form to simulate the experiment. Gary et al. (29) also compared their numerical results with this experiment. All the above results are plotted in Fig. 4.2 which shows the pressure profile. The experimental data for the saturation profile is not available, but the two sets of numerical results of saturation calculations are presented in Fig. 4.3. The core properties specifications are listed in Table 4.3.

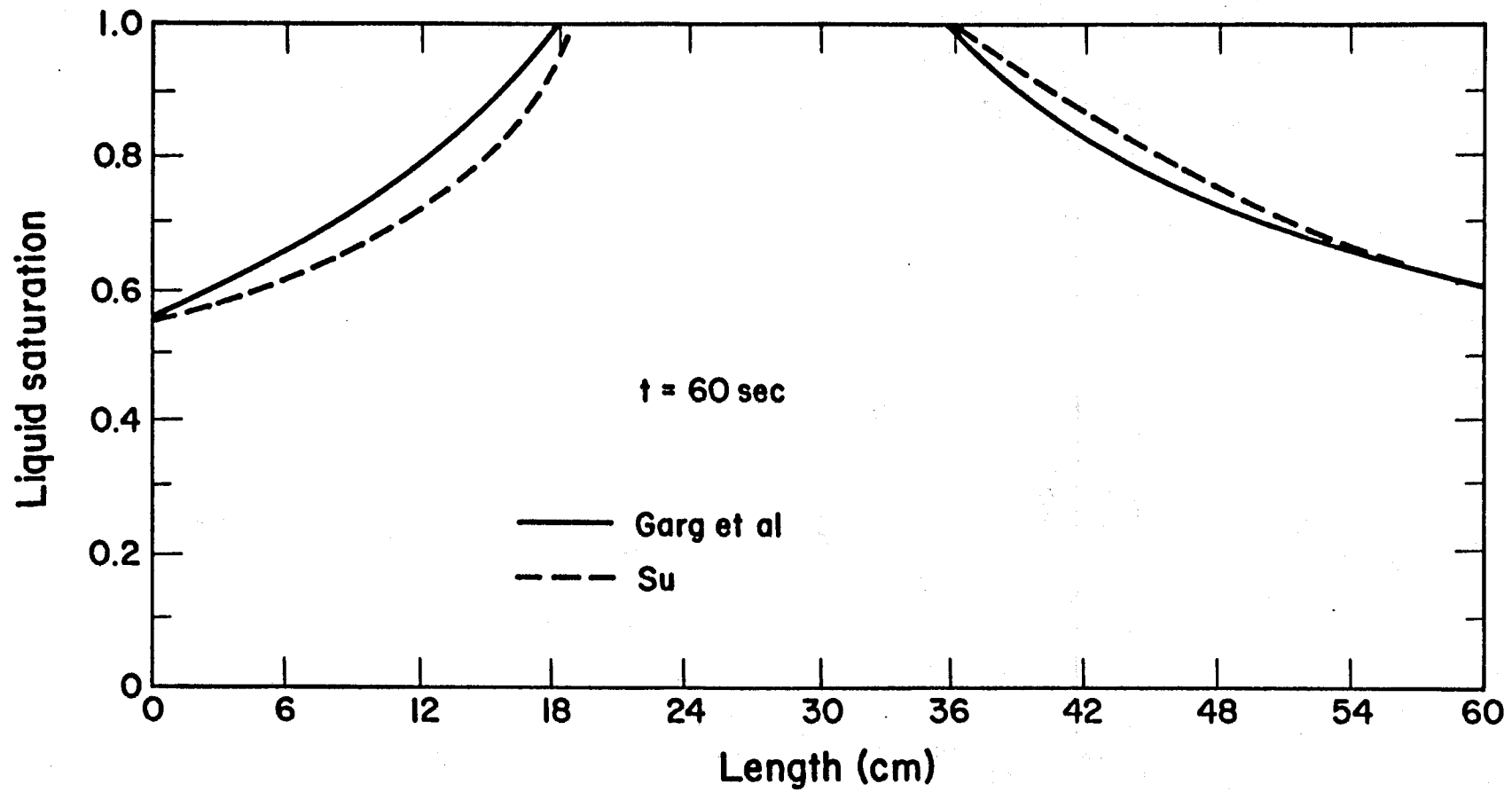
The three sets of results agree with each other very well. The pressure decreased rapidly until it approached the saturation pressure, and then the phase change phenomenon slowed down the rate of pressure decrease. The evaporation began at the left end due to the higher initial temperature at this end. Note that the capillary pressure effect is not included in this simulation.

The one-dimensional two-phase program was also



XBL 818-3478

Figure 4.2 Comparison of calculated pressure profiles with experimental data



XBL 818-3480

Figure 4.3 Comparison of calculated liquid saturation profiles

Table 4.3 Input specifications for simulation of  
Stanford experiment

Absolute permeability	0.10 darcys
Porosity	0.36
Formation specific heat	0.24 cal/gm <sup>o</sup> C
Grain density	2.65 gm/cm <sup>3</sup>
Pressure history at the right end	
p = 4.76 atm	t = 0 - 180 sec

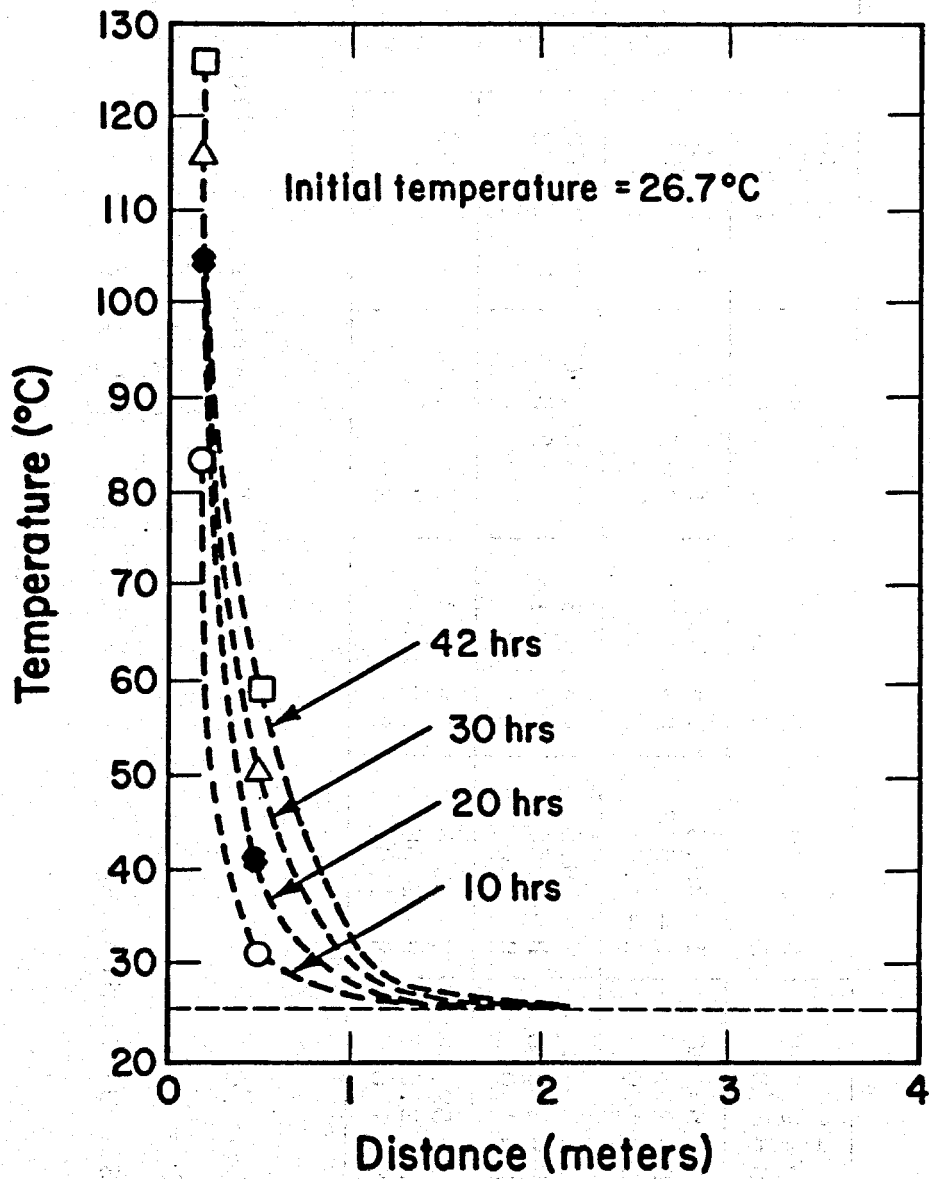
applied to the experiment in the present work as described in Chapter III, as a verification for the case when capillary pressure effect is included. There is also a good agreement between the experimental and numerical results as shown in Fig. 3.12.

#### IV.5. Numerical Results

With the input specifications described in Section IV.3, the simulation of the process around the wellbore and surrounding system generated reasonable results. The convergence was achieved in four to eight iterations. Evaporation begins in the first cell adjacent to the wellbore at 42 hours. The temperature history before evaporation is shown in Fig. 4.4. As expected, all the horizontal layers have the same temperature profile before evaporation begins.

Table 4.4 shows the results at 42.53 hours. The pressure build up due to phase change may be noted in cell (1,1). The grid cell identification notation, (i,j), shown in Fig. 4.1 is used for convenience. The strong convection from (1,1) to (1,2) makes the temperature at (1,2) higher than the temperature of the other grid cells in the same column. The grid point (1,1) has a lower temperature than the other cells in the first column, since most of the heat conducted from the wellbore is required for the phase change.

Table 4.5 shows the numerical results at 45.77 hours. At this time, all the grid cells in the first column are within the two-phase region. The rapid decrease in water



XBL 818-3485

Figure 4.4 Temperature history before evaporation starts

Table 4.4 Numerical results at 42.53 hours  
grid notation (i,j)

j	i							
		T = 126.9 P = 2.507 S = 0.965	T = 60.1 P = 2.503 S = 1.0	T = 29.8 P = 2.497 S = 1.0	T = 26.8 P = 2.490 S = 1.0	T = 26.66 P = 2.484 S = 1.0	T = 26.66 P = 2.479 S = 1.0	T = 26.66 P = 2.475 S = 1.0
		T = 127.1 P = 2.532 S = 1.0	T = 59.96 P = 2.530 S = 1.0	T = 29.8 P = 2.526 S = 1.0	T = 26.8 P = 2.519 S = 1.0	T = 26.66 P = 2.514 S = 1.0	T = 26.66 P = 2.509 S = 1.0	T = 26.66 P = 2.505 S = 1.0
		T = 127.1 P = 2.560 S = 1.0	T = 59.96 P = 2.558 S = 1.0	T = 29.8 P = 2.555 S = 1.0	T = 26.8 P = 2.549 S = 1.0	T = 26.66 P = 2.543 S = 1.0	T = 26.66 P = 2.538 S = 1.0	T = 26.66 P = 2.534 S = 1.0
		T = 127.1 P = 2.588 S = 1.0	T = 59.96 P = 2.587 S = 1.0	T = 29.8 P = 2.584 S = 1.0	T = 26.8 P = 2.578 S = 1.0	T = 26.66 P = 2.573 S = 1.0	T = 26.66 P = 2.568 S = 1.0	T = 26.66 P = 2.564 S = 1.0

Units =  $\left\{ \begin{array}{l} T = ^\circ\text{C} \\ P = \text{atm} \\ S = \text{dimensionless} \end{array} \right.$

T = temperature; S = liquid saturation  
 $P = \left\{ \begin{array}{l} P_v \text{ if } S < 1 \\ P_w \text{ if } S = 1 \end{array} \right.$

Table 4.5 Numerical results at 45.77 hours  
grid notation (i,j)

↓ j	→ i							
		T = 129.2 P = 2.688 S = 0.356	T = 66.6 P = 2.585 S = 1.0	T = 30.7 P = 2.576 S = 1.0	T = 26.8 P = 2.548 S = 1.0	T = 26.7 P = 2.520 S = 1.0	T = 26.66 P = 2.496 S = 1.0	T = 26.66 P = 2.475 S = 1.0
		T = 129.7 P = 2.736 S = 0.434	T = 66.2 P = 2.618 S = 1.0	T = 30.7 P = 2.608 S = 1.0	T = 26.8 P = 2.578 S = 1.0	T = 26.7 P = 2.549 S = 1.0	T = 26.66 P = 2.525 S = 1.0	T = 26.66 P = 2.505 S = 1.0
		T = 130.6 P = 2.811 S = 0.537	T = 65.9 P = 2.659 S = 1.0	T = 30.8 P = 2.641 S = 1.0	T = 26.8 P = 2.608 S = 1.0	T = 26.7 P = 2.579 S = 1.0	T = 26.66 P = 2.555 S = 1.0	T = 26.66 P = 2.534 S = 1.0
		T = 130.2 P = 2.778 S = 0.875	T = 65.5 P = 2.710 S = 1.0	T = 30.8 P = 2.675 S = 1.0	T = 26.8 P = 2.638 S = 1.0	T = 26.7 P = 2.608 S = 1.0	T = 26.66 P = 2.584 S = 1.0	T = 26.66 P = 2.564 S = 1.0

Units =  $\left\{ \begin{array}{l} T = ^\circ\text{C} \\ P = \text{atm} \\ S = \text{dimensionless} \end{array} \right.$

T = temperature; S = liquid saturation

$P = \left\{ \begin{array}{l} P_v \text{ if } S < 1 \\ P_w \text{ if } S = 1 \end{array} \right.$



saturation is not due to evaporation alone, but the water is also displaced by the pressure built up around the wellbore. The gravity effect is shown by the greater liquid saturation in the lower cells.

The last time step (302.8 hours) is shown in Table 4.6. Although the whole region has not reached steady state as yet, the grid cells in the first column seem to have reached steady temperature and saturation values. The water pressure distribution is shown in Table 4.7 from which some inward waterflow can be observed. Note from Table 4.6 that the water saturations in the first column are below irreducible water saturation.

To give more insight into the whole process, the temperature and saturation histories of grid cell (1,1) are plotted in Fig. 4.5. After evaporation begins, the water saturation value of grid cell (1,1) drops sharply until the phase change phenomenon occurs at the other grid cells of the first column. After all the saturation values of the grid cells in the first column have reached the irreducible water saturation value at about 90 hours, the saturation of grid cell (1,1) begins to show another sharp drop. Finally it reached a point at which the capillary pressure is large enough to bring some water back to maintain the liquid saturation value around 0.128.

It is also interesting to note that the two temperature changes after 42 hours occur at the same time as the sharp saturation changes. This is due to the pressure increasing as a result of the rapid phase change.

Table 4.6 Numerical results at 302.8 hours  
grid notation (i,j)

j	i							
		T = 133.5 P = 2.747 S = 0.129	T = 129.1 P = 2.679 S = 0.29	T = 127.6 P = 2.563 S = 0.859	T = 54.0 P = 2.537 S = 1.0	T = 30.7 P = 2.520 S = 1.0	T = 26.9 P = 2.497 S = 1.0	T = 26.66 P = 2.475 S = 1.0
		T = 133.1 P = 2.752 S = 0.130	T = 129.1 P = 2.685 S = 0.305	T = 123.9 P = 2.576 S = 1.0	T = 53.59 P = 2.566 S = 1.0	T = 30.6 P = 2.549 S = 1.0	T = 26.9 P = 2.526 S = 1.0	T = 26.66 P = 2.505 S = 1.0
		T = 133.0 P = 2.759 S = 0.131	T = 129.3 P = 2.695 S = 0.316	T = 119.2 P = 2.604 S = 1.0	T = 52.9 P = 2.595 S = 1.0	T = 30.6 P = 2.579 S = 1.0	T = 26.9 P = 2.556 S = 1.0	T = 26.66 P = 2.534 S = 1.0
		T = 132.7 P = 2.766 S = 0.133	T = 129.3 P = 2.704 S = 0.334	T = 115.4 P = 2.632 S = 1.0	T = 52.4 P = 2.625 S = 1.0	T = 30.6 P = 2.608 S = 1.0	T = 26.9 P = 2.585 S = 1.0	T = 26.66 P = 2.564 S = 1.0

Units =  $\left\{ \begin{array}{l} T = ^\circ\text{C} \\ P = \text{atm} \\ S = \text{dimensionless} \end{array} \right.$

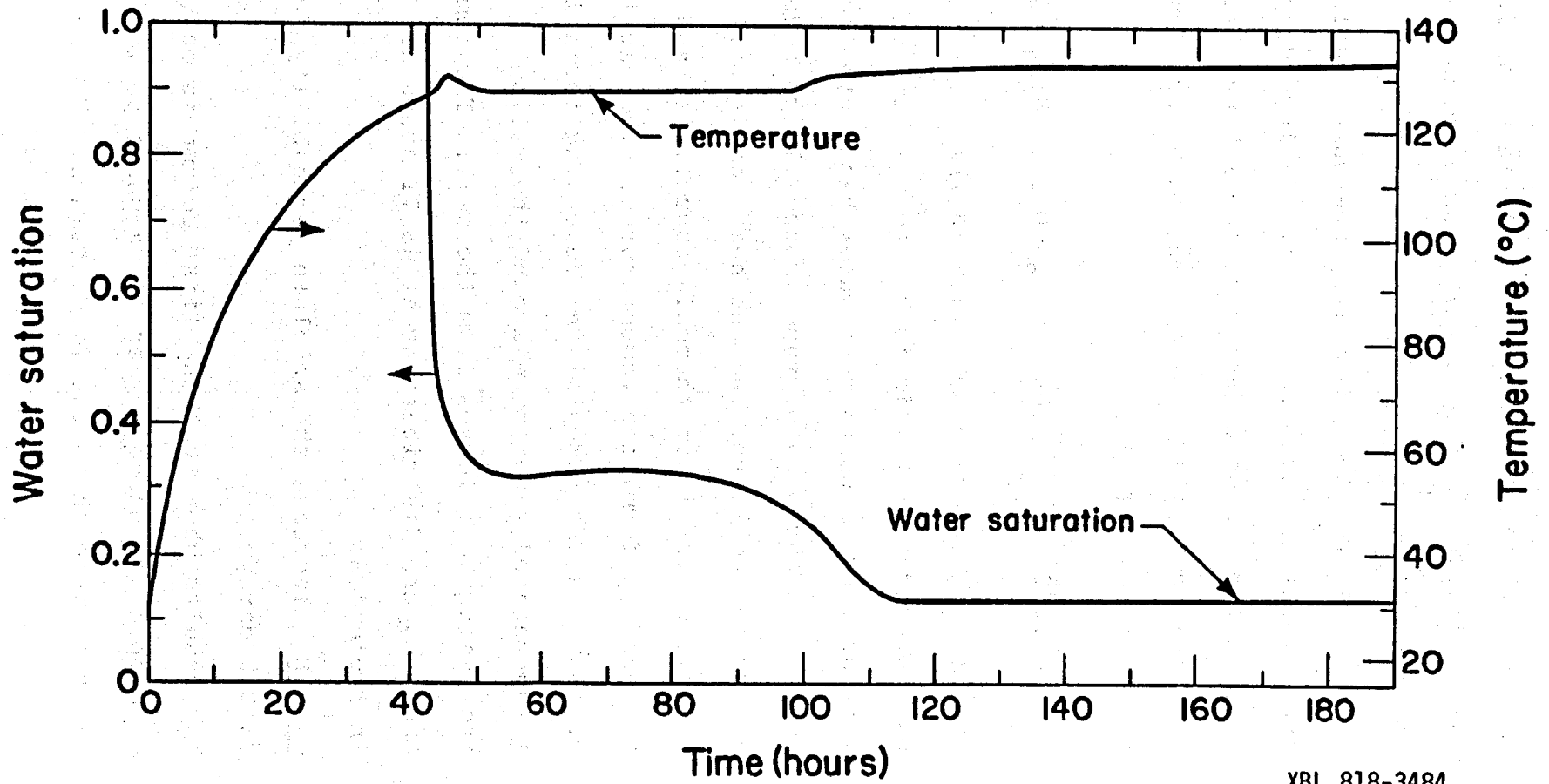
T = temperature; S = liquid saturation  
 $P = \left\{ \begin{array}{l} P_v \text{ if } S < 1 \\ P_w \text{ if } S = 1 \end{array} \right.$

Table 4.7 Water pressure distribution at 302.8 hours

grid notation (i,j)

	1.968	2.548	2.552	2.536	2.520	2.497	2.475
	1.984	2.577	2.576	2.566	2.549	2.526	2.505
	2.000	2.601	2.603	2.595	2.579	2.556	2.534
	2.018	2.629	2.632	2.625	2.608	2.585	2.564

Unit = atm



XBL 818-3484

Figure 4.5 Temperature and saturation histories of grid cell (1,1) for the standard case

It is worthwhile to study the effects of different input specifications. Some interesting conclusions can be made for the following cases:

Case A. Assume that capillary pressure equals zero. The saturation values in the first column drop faster than in the standard case. At 48.71 hours, all the grid points in the first column reach very low liquid saturations as follows:

$$S_{1,1} = 0.078; S_{1,2} = 0.095; S_{1,3} = 0.138; S_{1,4} = 0.183$$

The other grid cells are still in the fully water saturated region. This is due to the lack of capillary driving force to move water back into the first column. A superheated vapor zone will soon develop around the wellbore, and the heat losses will decrease because of the lower thermal conductivity and higher surrounding formation temperatures. The capillary pressure is instrumental in preventing formation of a superheated vapor zone around the wellbore, thus increasing heat losses from the well. The temperature and pressure distributions at 48.71 hours are shown in Table 4.8.

Case B. Increase the absolute permeability from 0.1 to 0.5 darcys.

The results show that the first column is only able to develop a two-phase region for a short period before water flows back to the first column. Figure 4.6

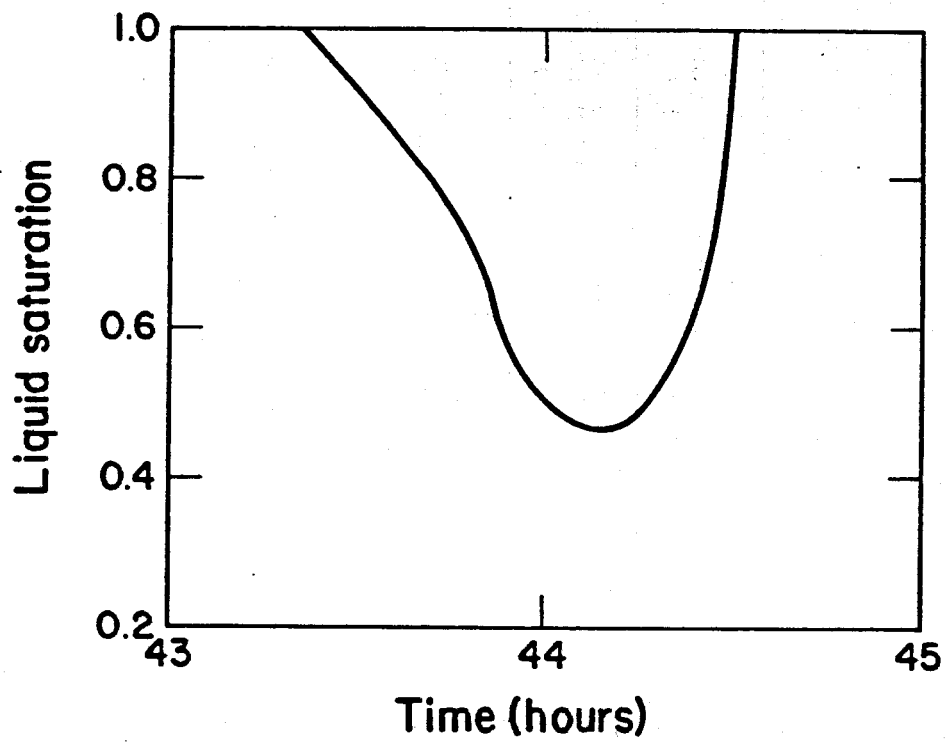
Table 4.8 Numerical results of case A at 48.71 hours  
grid notation (i,j)

i →							
↓ j	T = 139.3 P = 2.494 S = 0.078	T = 72.2 P = 2.489 S = 1.0	T = 31.2 P = 2.485 S = 1.0	T = 26.9 P = 2.482 S = 1.0	T = 26.7 P = 2.479 S = 1.0	T = 26.67 P = 2.477 S = 1.0	T = 26.66 P = 2.475 S = 1.0
	T = 127.0 P = 2.539 S = 0.095	T = 72.4 P = 2.523 S = 1.0	T = 31.3 P = 2.515 S = 1.0	T = 26.9 P = 2.511 S = 1.0	T = 26.7 P = 2.508 S = 1.0	T = 26.67 P = 2.506 S = 1.0	T = 26.66 P = 2.505 S = 1.0
	T = 129.8 P = 2.580 S = 0.138	T = 72.7 P = 2.553 S = 1.0	T = 31.3 P = 2.545 S = 1.0	T = 26.9 P = 2.541 S = 1.0	T = 26.7 P = 2.538 S = 1.0	T = 26.67 P = 2.536 S = 1.0	T = 26.66 P = 2.534 S = 1.0
	T = 128.7 P = 2.609 S = 0.183	T = 73.1 P = 2.582 S = 1.0	T = 31.4 P = 2.575 S = 1.0	T = 26.9 P = 2.571 S = 1.0	T = 26.7 P = 2.568 S = 1.0	T = 26.67 P = 2.566 S = 1.0	T = 26.66 P = 2.564 S = 1.0

Units = {  
 T = °C  
 P = atm  
 S = dimensionless

T = temperature; S = liquid saturation  

$$P = \begin{cases} P_v & \text{if } S < 1 \\ P_w & \text{if } S = 1 \end{cases}$$



XBL 818-3481

Figure 4.6 Saturation variation of grid point (1,4)

shows the variation of saturation with time for grid cell (1,4) to demonstrate this process. The above process can be explained as follows. In the initial stage of evaporation, there is a pressure increase in the cells around the wellbore due to the phase change. However, this pressure increase effect due to the phase change will become smaller at later times when the water saturations in these cells decrease. Meanwhile there is an outgoing flow from the cells around the wellbore to the cells away from the wellbore due to a pressure gradient and this outgoing flow will decrease the pressure of the cells around the wellbore. In this case, the high permeability value will create a situation where the pressure decreasing effect due to the outgoing flow can overcome the pressure increasing effect from the phase change. Thus, the pressure of the cells around the wellbore will decline to a value at which the water can flow back towards the wellbore by capillary force. The numerical results at 44.4 hours are shown in Table 4.9.

Case C. Decrease absolute permeability from 0.1 to 0.05 darcys.

The temperature and saturation histories in cell (1,1) are shown in Fig. 4.7. In this case, a two-phase region is developed similar to the standard case, but with higher temperature and lower water saturation at the final simulation time. As shown



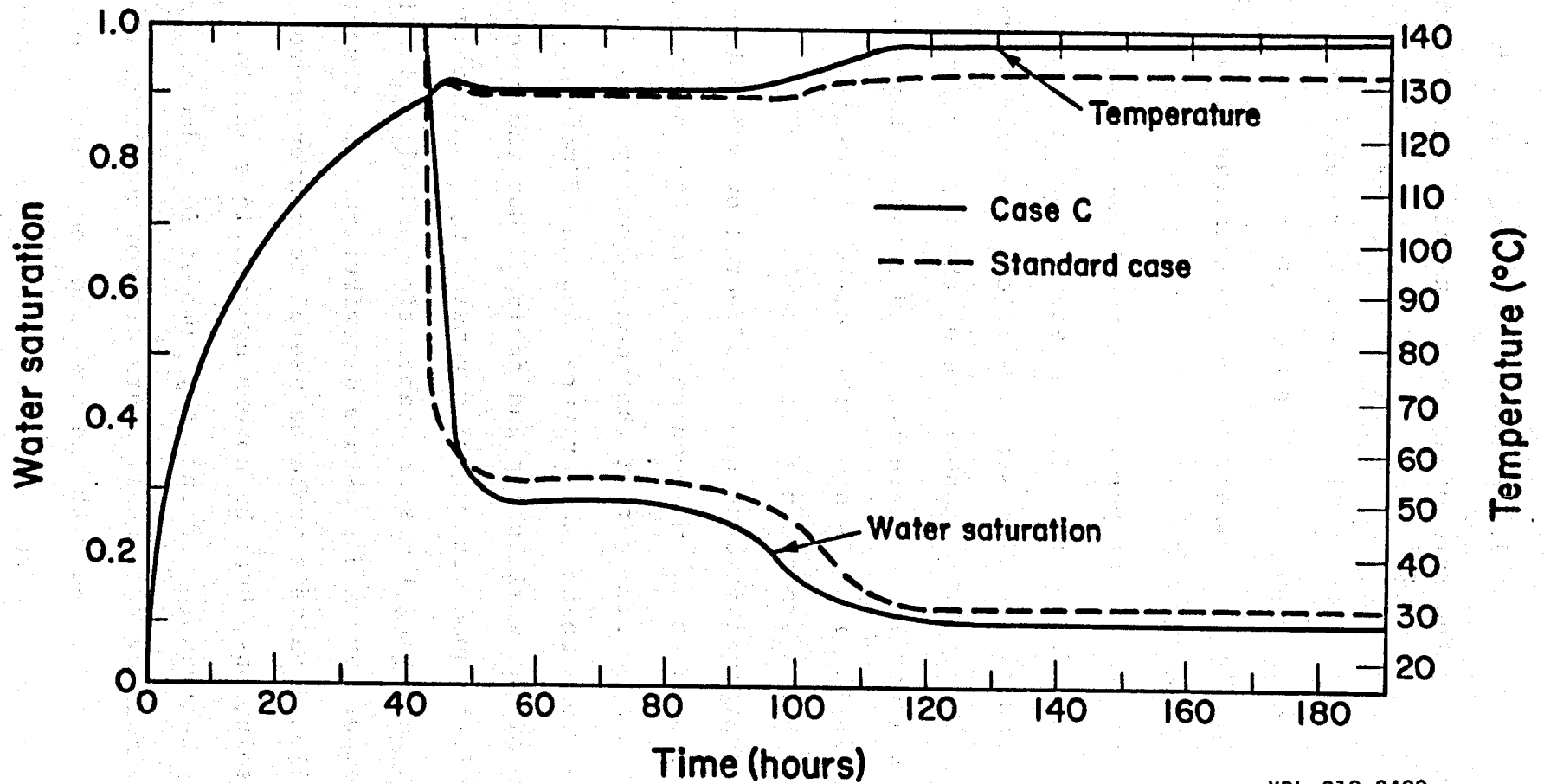
Table 4.9 Numerical results of case B at 44.4 hours  
grid notation (i,j)

j	i							
		T = 126.4 P = 2.469 S = 0.40	T = 67.1 P = 2.415 S = 1.0	T = 30.5 P = 2.423 S = 1.0	T = 26.8 P = 2.439 S = 1.0	T = 26.7 P = 2.453 S = 1.0	T = 26.7 P = 2.465 S = 1.0	T = 26.7 P = 2.475 S = 1.0
		T = 126.7 P = 2.491 S = 0.48	T = 66.1 P = 2.441 S = 1.0	T = 30.5 P = 2.452 S = 1.0	T = 26.8 P = 2.468 S = 1.0	T = 26.7 P = 2.483 S = 1.0	T = 26.7 P = 2.495 S = 1.0	T = 26.7 P = 2.505 S = 1.0
		T = 126.7 P = 2.493 S = 0.48	T = 66.2 P = 2.464 S = 1.0	T = 30.5 P = 2.480 S = 1.0	T = 26.8 P = 2.500 S = 1.0	T = 26.7 P = 2.483 S = 1.0	T = 26.7 P = 2.524 S = 1.0	T = 26.7 P = 2.534 S = 1.0
		T = 126.0 P = 2.438 S = 0.60	T = 66.6 P = 2.480 S = 1.0	T = 30.6 P = 2.507 S = 1.0	T = 26.8 P = 2.527 S = 1.0	T = 26.7 P = 2.453 S = 1.0	T = 26.7 P = 2.554 S = 1.0	T = 26.7 P = 2.564 S = 1.0

Units =  $\left\{ \begin{array}{l} T = ^\circ\text{C} \\ P = \text{atm} \\ S = \text{dimensionless} \end{array} \right.$

T = temperature; S = liquid saturation

$P = \left\{ \begin{array}{l} P_v \text{ if } S < 1 \\ P_w \text{ if } S = 1 \end{array} \right.$



XBL 818-3483

Figure 4.7 Temperature and saturation histories of grid cell (1,1) for the case C ( $k = .05$  darcys)

in Fig. 4.7, the lower absolute permeability value slows down the rate of decrease in water saturation due to the smaller outgoing water flow rate when evaporation first begins. Numerical results at 45.77 hours are shown in Table 4.10.

Case D. Increase the injection temperature from  $315.6^{\circ}\text{C}$  to  $426.7^{\circ}\text{C}$ .

As expected the temperature in the first column increased faster than for the standard case, and the evaporation also starts earlier, at 16.19 hours. Compared with the standard case, the first column has a lower liquid saturation and a higher temperature in the final state. The numerical results at 45.83 hours are shown in Table 4.11.

The numerical results can be affected by other input parameters such as thermal conductivity of the formation, density and specific heat of the rock, porosity, initial formation pressure and temperature, and the dimensions and materials of the well tubing and casing. But the general pattern of the numerical results remains the same, only the different beginning times of evaporation and slightly different temperature and pressure distributions are observed. Dimensionless analysis would be useful to achieve more general solutions, but the governing equations in this work could not be transformed into any simpler form due to the fact that most of the coefficients are not constant, the equations are coupled with the pressure-temperature relation of the steam table, and no independent dimensionless

Table 4.10 Numerical results of case C at 45.77 hours

grid notation (i,j)

j	i							
		T = 130.9 P = 2.828 S = 0.475	T = 64.3 P = 2.614 S = 1.0	T = 30.6 P = 2.560 S = 1.0	T = 26.8 P = 2.564 S = 1.0	T = 26.7 P = 2.529 S = 1.0	T = 26.7 P = 2.500 S = 1.0	T = 26.7 P = 2.475 S = 1.0
		T = 130.8 P = 2.828 S = 0.677	T = 64.5 P = 2.654 S = 1.0	T = 30.6 P = 2.632 S = 1.0	T = 26.8 P = 2.595 S = 1.0	T = 26.7 P = 2.559 S = 1.0	T = 26.7 P = 2.530 S = 1.0	T = 26.7 P = 2.505 S = 1.0
		T = 129.5 P = 2.715 S = 0.993	T = 63.4 P = 2.692 S = 1.0	T = 30.5 P = 2.663 S = 1.0	T = 26.8 P = 2.623 S = 1.0	T = 26.7 P = 2.588 S = 1.0	T = 26.7 P = 2.559 S = 1.0	T = 26.7 P = 2.534 S = 1.0
		T = 129.3 P = 2.730 S = 1.0	T = 62.8 P = 2.72 S = 1.0	T = 30.5 P = 2.693 S = 1.0	T = 26.8 P = 2.653 S = 1.0	T = 26.7 P = 2.618 S = 1.0	T = 26.7 P = 2.589 S = 1.0	T = 26.7 P = 2.564 S = 1.0

Units = {  
 T = °C  
 P = atm  
 S = dimensionless

T = temperature; S = liquid saturation  

$$P = \begin{cases} P_v & \text{if } S < 1 \\ P_w & \text{if } S = 1 \end{cases}$$

Table 4.11 Numerical results of case D at 45.83 hours  
grid notation (i,j)

i →							
↓ j	T = 129.0 P = 2.695 S = 0.265	T = 127.2 P = 2.529 S = 0.959	T = 35.2 P = 2.522 S = 1.0	T = 27.0 P = 2.509 S = 1.0	T = 26.7 P = 2.496 S = 1.0	T = 26.7 P = 2.485 S = 1.0	T = 26.7 P = 2.475 S = 1.0
	T = 129.4 P = 2.709 S = 0.300	T = 119.4 P = 2.553 S = 1.000	T = 35.0 P = 2.551 S = 1.0	T = 27.0 P = 2.539 S = 1.0	T = 26.7 P = 2.525 S = 1.0	T = 26.7 P = 2.514 S = 1.0	T = 26.7 P = 2.505 S = 1.0
	T = 129.7 P = 2.732 S = 0.273	T = 127.9 P = 2.588 S = 0.952	T = 27.0 P = 2.581 S = 1.0	T = 26.7 P = 2.568 S = 1.0	T = 26.7 P = 2.555 S = 1.0	T = 26.7 P = 2.544 S = 1.0	T = 26.7 P = 2.534 S = 1.0
	T = 129.9 P = 2.747 S = 0.279	T = 128.3 P = 2.614 S = 0.990	T = 34.7 P = 2.610 S = 1.0	T = 27.0 P = 2.598 S = 1.0	T = 26.7 P = 2.584 S = 1.0	T = 26.7 P = 2.573 S = 1.0	T = 26.7 P = 2.564 S = 1.0

Units =  $\left\{ \begin{array}{l} T = ^\circ\text{C} \\ P = \text{atm} \\ S = \text{dimensionless} \end{array} \right.$

T = temperature; S = liquid saturation

$P = \left\{ \begin{array}{l} P_v \text{ if } S < 1 \\ P_w \text{ if } S = 1 \end{array} \right.$

form of the set of governing equations will be identical, in a mathematical sense, for different application cases. Hence the dimensionless analysis was not performed here.

#### IV.6. Applications

The following equation can be used for calculating the wellbore heat losses per unit length of wellbore:

$$Q = U_o (T_w - T) 2\pi r$$

In the numerical simulation, the wellbore inside temperature is kept at a constant value which is also the case in practice. The heat losses will change the quality of the injected steam, but the steam temperature essentially remains a constant value subject to a nearly constant pressure inside the wellbore. Also the overall heat transfer coefficient,  $U_o$ , is a very weak function of formation temperature. Therefore, the heat losses will be determined by the temperature surrounding the wellbore.

Usually wellbore heat loss calculations only consider single phase heat conduction. This calculation would indicate a higher formation temperature around the wellbore in the region in which a two-phase mixing zone could be developed. For example, the final surrounding temperature from the single-phase calculation will reach  $176.6^{\circ}\text{C}$  for a constant wellbore temperature of  $315.6^{\circ}\text{C}$ , while the lowest surrounding temperature, considering phase changes, will be  $100^{\circ}\text{C}$  at depths near the surface. In such a case, the maximum error in the heat losses calculations could be

up to 50 percent.

Since the saturation temperature increases as the pressure increases, the formation of a two-phase zone will be suppressed in deeper formations by a higher formation fluid pressure. The phase change phenomenon will not occur, if the surrounding formation temperature from the single-phase heat conduction calculation is lower than the saturation temperature. If the formation fluid pressure can be approximated by the hydrostatic pressure, then the maximum depth possible for formation of a two-phase mixing zone is listed in Table 4.12 according to different injection temperatures. The maximum surrounding formation temperatures in the above table are taken from the numerical results of the computer program developed in this work with the single-phase option. Therefore, the influence of the heat pipe effect in wellbore heat losses is limited. It may have a significant effect for the shallow formations but it will have little or no effect in deep formations.

**Table 4.12 The maximum possible depths of a two-phase zone developed around the wellbore**

<b>Injection steam temperature</b>	<b>Maximum formation temperature</b>	<b>Depth</b>
204.4°C	110.0°C	4.3 meters
315.6°C	176.6°C	84.3 meters
426.6°C	235.4°C	301.2 meters



## CHAPTER V. CONCLUSIONS

1. The one-dimensional experiment has confirmed that there may be a heat pipe effect in a partially liquid saturated porous medium.
2. The occurrence of the heat pipe phenomenon can cause significant changes in the apparent thermal conductivity of a partially liquid saturated porous medium and thus greatly increase the magnitude of heat flux for a given temperature differential.
3. A one-dimensional steady state theory has been developed which describes the functional dependence of the heat pipe phenomenon on liquid saturation gradient, capillary pressure, permeability, viscosity, latent heat, heat flux and gravity. Calculation of the amount of water displaced from the system at equilibrium conditions, using the mathematical solution of the theory, is in reasonable agreement with the experimental data.
4. A two-dimensional two-phase program has been developed to calculate the heat losses from a steam injection well or a geothermal production well. The simulation results show that a two-phase region is likely to be developed around a wellbore with the depth not too far from the surface for typical underground formation properties. The water saturation of the formation nearest the wellbore may be reduced below the irreducible point, but the vapor pressure lowering effect and capillary pressure will

prevent formation of a completely dry region. Under this condition, the heat losses from the wellbore will increase because of the lower surrounding formation temperature due to the heat pipe effect.

5. If the capillary pressure can be neglected and the absolute permeability is not too high, then a superheated vapor zone will be formed around the wellbore. That will result in a reduction of heat losses from the wellbore.

6. The numerical results show that permeability is an important parameter in formation of a two-phase zone. In a very high permeability formation, the pressure built up around the wellbore from phase changes, declines quickly due to greater outgoing flow rate. Then the water will be easily drawn back to the two-phase region by capillary pressure. A stable two-phase zone cannot be developed around the wellbore for this case. On the other hand, for low permeability formations higher pressure will be built up in the two-phase region around the wellbore due to a smaller outgoing flow rate. This results in a higher surrounding temperature around the wellbore.

7. The two-phase region will be suppressed by higher hydrostatic pressure of the formation fluids and can exist between the surface and 84 meters depth for an injection temperature of  $315^{\circ}\text{C}$ . Consideration of phase changes is probably only important for shallower formations.

## NOMENCLATURE

$g$	gravity in vector form
$h_{fg}$	latent heat of vaporization
$h_w$	enthalpy of water
$h_v$	enthalpy of vapor
$J_g$	heat flux in non-equilibrium thermodynamics approach
$K$	absolute permeability
$k_w$	relative permeability to water
$k_v$	relative permeability to vapor
$L$	length of system
$L_{qq}$	phenomenological coefficient
$\hat{m}_v$	mass flux of vapor phase in vector form
$\hat{m}_w$	mass flux of water phase in vector form
$\bar{m}$	average mass flux
$P_c$	capillary pressure
$P_v$	vapor pressure
$P_w$	water pressure
$Q$	heat flux
$Q_c$	condensation or evaporation term
$r_{to}$	outside radius of tubing
$r_h$	well bore radius
$S_w$	water saturation
$S_v$	vapor saturation
$S_{ig}$	irreducible gas saturation
$S_{iw}$	irreducible water saturation

$T$	temperature
$T_w$	wellbore inside temperature
$T_s$	saturation temperature
$U$	internal energy
$U_o$	overall heat transfer coefficient
$\phi$	porosity
$\rho_w$	water density
$\rho_v$	vapor density
$(\rho C_p)_{\text{rock}}$	volumetric heat capacity of rock
$\nu$	kinematic viscosity
$\mu$	dynamic viscosity
$\delta P$	vapor pressure change between time steps
$\delta S_w$	liquid saturation change between time steps
$\delta T$	temperature change between time steps
$\lambda$	thermal conductivity
$\lambda_a$	apparent thermal conductivity
$\lambda_{HP}$	heat pipe effect contribution to thermal conductivity

REFERENCES

1. Gomma, E. E. and Somerton, W. H.: "Thermal Behavior of Multifluid-Saturated Formations, Part II: Effect of Vapor Saturation-Heat Pipe Concept and Apparent Thermal Conductivity," Paper No. SPE 4896-B presented at the SPE-AIME 44th Annual California Regional Meeting, San Francisco, April 4-5, 1974.
2. Gomma, E. E.: "Thermal Behavior of Partially Liquid Saturated Porous Media," Ph.D. Thesis, University of California, Berkeley, 1973.
3. Schrock, V. E., Fernandez, R. T., and Kesaran, K.: "Heat Transfer From Cylinders Embedded in a Liquid Filled Porous Medium," Paper CT3.6, Proc. of 4th Internal. Heat Transfer Conference, Paris-Versailles, 1970.
4. Grover, G. M., Cotter, T. P., and Erickson, J.: "Structure of Very High Conductance," J. of Applied Physics, Vol. 35, 1964, p. 1990.
5. Cotter, T. P.: "Theory of Heat Pipe," Report No. LA-3246-MS, Los Alamos Scientific Laboratory, 1965.
6. Tien, C. L.: "Two Component Heat Pipes," Progress in Astronautics and Aeronautics, Vol. 23, 1970, p. 423.
7. Sun, K. H.: Ph.D. Thesis, University of California, Berkeley, 1973.
8. Boyoucos, G. J.: "The Effect of Temperature on the Movement of Water Vapor and Capillary Moisture in Soils," Journal of Agriculture Research, Vol. 5, 1915, pp. 141-172.
9. Winterkorn, H. F.: "Fundamental Similarities Between Electro-Osmotic and Thermo-Osmotic Phenomena," Highway Research Board Proceedings, Vol. 27, 1947, pp. 443-455.
10. Taylor, S. A., and Cavazza, L.: "The Movement of Soil Moisture in Response to Temperature Gradients," Soil Science Society of America Proceedings, Vol. 18, No. 4, 1954, pp. 351-365.

11. Philip, J. R., and de Vries, D. A.: "Moisture Movement in Porous Materials Under Temperature Gradients," Transactions American Geophysical Union, Vol. 38, No. 2, 1957, pp. 222-232.
12. de Vries, D. A.: "Simultaneous Transfer of Heat and Moisture in Porous Media," Transactions American Geophysical Union, Vol. 39, No. 5, 1958, pp. 909-916.
13. Valchar, J.: "Heat Moisture Transfer in Capillary Porous Body From the Point of View of the Thermodynamics of Irreversible Process," Proceedings of the Third International Heat Transfer Conference, Chicago, August 1966, Vol. 1, pp. 409-418.
14. Cary, J. W.: "An Evaporation Experiment and its Irreversible Thermodynamics," International Journal of Heat and Mass Transfer, Vol. 7, 1964, pp. 531-538.
15. Hansen, D., Breyer, W. H., and Riback, W. J.: "Steady State Heat Transfer in Partially Liquid Filled Porous Media," Transactions of the ASME, August 1970, pp. 520-527.
16. Keenan, J. H.: "Thermodynamics," John Wiley and Sons, 1952.
17. Muskat, M., and Meres, M. W., Physics, Vol. 7, 1936, pp. 346.
18. Chen, H. K., Counsil, J. R., and Ramey, H. J.: "Experimental Steam-Water Relative Permeability Curves," Transaction of Geothermal Resources Council, Vol. 2, July 1978.
19. Kar, K., and Dybbs, A.: "Effective Thermal Conductivity of Fully and Partially Saturated Metal Wicks," Proceedings of the Sixth International Heat Transfer Conference, Vol. 3, August 1978, pp. 91-97.
20. Calhoun, J. C., Lewis, M., and Newman, R. C.: "Experiments on the Capillary Properties of Porous Solids," Transactions, AIME, July 1949, pp. 189-191.
21. Chen, H. K.: "Measurement of Water Content in Porous Media Under Geothermal Fluid Flow Conditions," Ph.D. Thesis, Stanford University, December 1976.
22. Corey, A. T., Rathjens, C. H., Henderson, J. H., and Wyllie, R. J.: "Three-Phase Relative Permeability," Transactions, AIME, Vol. 207, 1956, pp. 349.

23. Castor, T.: "Enhanced Recovery of Acidic Oils by Alkaline Agents," Ph.D. Thesis, University of California, Berkeley, 1979.
24. Ramey, H. J., Jr.: "Wellbore Heat Transmission," Journal of Petroleum Technology, Vol. 14, April 1962, pp. 427-435.
25. Leutwyler, K.: "Casing Temperature Studies in Steam Injection Wells," Journal of Petroleum Technology, September 1966, pp. 1157-1162.
26. Willhite, G. P.: "Overall Heat Transfer Coefficients in Steam and Hot Water Injection Wells," Journal of Petroleum Technology, Vol. 19, May 1967, pp. 607-615.
27. Shutler, N. D.: "Numerical, Three-Phase Simulation of the Linear Steamflood Process," Transactions, AIME, Vol. 246,
28. Mercer, J. W., and Faust, C. R.: "Simulation of Water Flow and Vapor-Dominated Hydrothermal Reservoirs," Paper SPE 5520 presented at SPE-AIME 50th Annual Fall Technical Conference and Exhibition, Dallas, September 1975.
29. Garg, S. K., Pritchitt, J. W., and Brownell, D. H., Jr.: "Transport of Mass and Energy in Porous Media," Paper presented at the Second United Nations Symposium on the Development and Use of Geothermal Resources, San Francisco, May 1975.
30. Lasseter, T. J., Witherspoon, P. A., and Lippmann, M. J.: "Multiphase Multidimensional Simulation of Geothermal Reservoirs," Second United Nations Symposium on the Development and Use of Geothermal Resources, San Francisco, May 1975.
31. Atkinson, P. G.: "Numerical Simulation of Two-Phase Boiling Flow in a Linear Horizontal Porous Medium," Report No. SGP-TR-18, Stanford Geothermal Program, Stanford University, December 1975.
32. Faust, C. R., and Mercer, J. W.: "A Comparison of Finite-Difference and Finite-Element Techniques Applied to Geothermal Reservoir Simulation," Paper SPE 5742 presented at SPE-AIME Fourth Symposium on Numerical Simulation of Reservoir Performance, Los Angeles, February 1976.
33. Coats, K. H., George, W. D., and Chu, C.: "Three-Dimensional Simulation of Steam-Flooding," Transactions, AIME, Vol. 257

34. Thomas, L. K., and Pierson, R. G.: "Three-Dimensional Geothermal Reservoir Simulation," Soc. Pet. Eng. Journal, April 1978, pp. 151-161.
35. Moench, A. F., and Herkelrath, W. N.: "The Effect of Vapor-Pressure Lowering Upon Pressure Drawdown and Buildup in Geothermal Steam Wells," Transaction of Geothermal Resources Council, Vol. 2, July 1978.
36. Somerton, W. H., Keese, J. A., and Chu, S. L.: "Thermal Behavior of Unconsolidated Oil Sands," Soc. Pet. Eng. Journal, Vol. 14, No. 5, 1974, pp. 513.
37. Baumeister, T.: "Mark's Standard Handbook for Mechanical Engineers," Eighth Edition, McGraw-Hill Book Company, 1978.
38. Aziz, K.: "Course Notes from Seminar on Reservoir Simulation," Course No. 273, Department of Petroleum Engineering, Stanford University, 1971.
39. Lasseter, T. J., and Witherspoon, P. A.: "Underground Storage of Liquefied Natural Gas in Cavities Created by Nuclear Explosives," Dept. of Civil Engineering, Institute of Transportation and Traffic Engineering Publication No. 74-1 (1974), University of California, Berkeley.
40. Blair, P. M., Peaceman, D. W., and Stone, H. W.: "Discussion of 'Use of Irregular Grid by Cylindrical Coordinates,' by A. Settari, K. Aziz," Soc. of Pet. Eng. Journal, August 1974, pp. 396.
41. Bruce, W. A., and Welge, H. J.: "Restored State Method for Determination of Oil in Place and Connate Water," Oil and Gas Journal, July 1947, pp. 223-238.
42. Kruger, P., and Ramey, H. J., Jr.: "Stimulation and Reservoir Engineering of Geothermal Resources," Report No. SGP-TR-1, Stanford University, June 1974.



## APPENDIX A. DERIVATION OF TRANSFORMATION EQUATIONS

(1) Derivation of Eqs. (4.5), (4.6) and their coefficients.

Equation (4.4) can be expanded as

$$\begin{aligned}
 \nabla \cdot \left\{ \frac{Kk_w}{v_w} [\nabla(P_v^{n+1} - P_v^n) + P_c^n - P_c^{n+1} + (\nabla P_w^n - \rho_w \hat{g})] \right\} \\
 + \nabla \cdot \left\{ \frac{Kk_v}{v} [\nabla(P_v^{n+1} - P_v^n) + \nabla P_v^n - \rho_v \hat{g}] \right\} \\
 = \phi \frac{\partial}{\partial t} (\rho_w S_w + \rho_v S_v) \quad (A.1)
 \end{aligned}$$

And  $\frac{\partial}{\partial t} (\rho_w S_w)$  can be expressed as

$$\begin{aligned}
 [(\rho_w^{n+1} S_w^{n+1}) - (\rho_w^n S_w^n)] \frac{1}{\Delta t} \\
 = [\rho_w^{n+1} (S_w^{n+1} - S_w^n) + S_w^n (\rho_w^{n+1} - \rho_w^n)] \frac{1}{\Delta t} \\
 = [\rho_w^{n+1} \delta S_w + S_w^n \delta \rho_w] \frac{1}{\Delta t}
 \end{aligned}$$

Then,

$$\begin{aligned}
 \nabla \cdot \left\{ \frac{Kk_w}{v_w} \nabla \delta P \right\} + \nabla \cdot \left\{ \frac{Kk_w}{v_w} [-\delta P_c + \nabla P_w^n - \rho_w \hat{g}] \right\} \\
 + \nabla \cdot \left\{ \frac{Kk_v}{v} \nabla \delta P \right\} + \nabla \cdot \left\{ \frac{Kk_v}{v} (\nabla P_v^n - \rho_v \hat{g}) \right\} \\
 = \frac{\phi}{\Delta t} (\rho_w^{n+1} - \rho_v^{n+1}) \delta S_w \phi \delta \rho_w - S_v^n \phi \delta \rho_v \quad (A.2)
 \end{aligned}$$

If water density is considered constant, then  $\delta \rho_w = 0$ .

$\delta \rho_v$  can be expanded as

$$\delta \rho_v = \frac{\partial \rho_v}{\partial P_v} \delta P + \frac{\partial \rho_v}{\partial T} \delta T .$$

Since the vapor density can be represented by a function of vapor pressure alone as shown in Chapter IV, then

$$\delta \rho_v = \frac{\partial \rho_v}{\partial P_v} \delta P .$$

Therefore, Eq. (B.2) can be rearranged as

$$\begin{aligned} \nabla \cdot \left\{ \left( \frac{Kk_w}{v_w} + \frac{Kk_v}{v_v} \right) \nabla \delta P \right\} + \nabla \left\{ \frac{Kk_w}{v_w} [\nabla P_w^n - \delta P_c - \rho_w \hat{g}] \right\} \\ + \nabla \left\{ \frac{Kk_v}{v_v} (\nabla P_v^n - \rho_v \hat{g}) \right\} = \frac{\phi}{\Delta t} (\rho_w^{n+1} - \rho_v^{n+1}) \delta S_w \\ - S_v^n \phi \frac{\partial \rho_v}{\partial P_v} \frac{1}{\Delta t} \delta P . \end{aligned}$$

This is identical with Eq. (4.5). In a similar way, Eq. (4.6) can be derived.

(2) Derivation of Eq. (4.8) and its coefficients.

Multiply Eq. (4.5) by  $-\frac{C_{21}}{C_{11}}$  and then add Eq. (4.6),

$$\begin{aligned} -\frac{C_{21}}{C_{11}} \nabla [(\tau_w + \tau_v) \nabla \delta P] + \nabla \tau_H \nabla \delta P = \left( -\frac{C_{12}}{C_{11}} C_{21} + C_{22} \right) \delta T \\ + \left( -\frac{C_{13}}{C_{11}} C_{21} + C_{23} \right) \delta P - \frac{R_1 \cdot C_{21}}{C_{11}} + R_2 \end{aligned} \quad (\text{A.3})$$

Multiply Eq. (4.5) by  $-\frac{C_{31}}{C_{11}}$  and add Eq. (4.7),

$$\begin{aligned} -\frac{C_{31}}{C_{11}} \nabla [(\tau_w + \tau_v) \nabla \delta P] = \left( -\frac{C_{12}}{C_{11}} C_{31} + C_{32} \right) \delta T \\ + \left( -\frac{C_{13}}{C_{11}} C_{31} + C_{33} \right) \delta P + R_3 - R_1 \frac{C_{31}}{C_{11}} . \end{aligned} \quad (\text{A.4})$$

Multiply Eq. (B.3) by  $-\frac{(-\frac{C_{12}}{C_{11}}C_{31} + C_{32})}{(-\frac{C_{12}}{C_{11}}C_{21} + C_{22})}$  and add Eq. (B.4),

$$\begin{aligned}
 & -(\nabla\tau_H \nabla\delta P - \frac{C_{21}}{C_{11}} \cdot \nabla[(\tau_w + \tau_v) \nabla\delta P]) \cdot [C_{32} - \frac{C_{12}}{C_{11}} C_{31}] / [C_{22} - \frac{C_{12}}{C_{11}} C_{21}] \\
 & + \nabla[(\tau_w + \tau_v) \delta P] \cdot (-\frac{C_{31}}{C_{11}}) = \{-[-\frac{C_{13}}{C_{11}} C_{21} + C_{23}] \cdot [-\frac{C_{12}}{C_{11}} C_{31} + C_{32}] / \\
 & [-\frac{C_{12}}{C_{11}} C_{21} + C_{22}] + [-\frac{C_{13}}{C_{11}} C_{31} + C_{33}] \} \delta P + R_3 - R_1 \frac{C_{31}}{C_{11}} \\
 & - (R_3 - \frac{R_1 C_{21}}{C_{11}}) \cdot [C_{32} - \frac{C_{12}}{C_{11}} C_{31}] / [-\frac{C_{12}}{C_{11}} C_{21} + C_{22}] \quad (A.5)
 \end{aligned}$$

Multiply the above equation by  $[-\frac{C_{12}}{C_{11}} C_{21} + C_{22}] C_{11}^2$  and rearrange,

$$\begin{aligned}
 & -[C_{11} \nabla\tau_H \nabla\delta P - C_{21} \nabla[(\tau_w + \tau_v) \nabla\delta P]] \cdot [C_{32} C_{11} - C_{12} C_{31}] \\
 & + C_{31} \cdot [-\nabla(\tau_w + \tau_v) \nabla\delta P] \cdot [C_{22} C_{11} - C_{12} C_{21}] \\
 & = \{-[C_{23} C_{11} - C_{13} C_{21}] \cdot [C_{32} C_{11} - C_{12} C_{31}] + [C_{33} C_{11} - C_{13} C_{31}] \\
 & \cdot [C_{22} C_{11} - C_{12} C_{21}]\} \cdot \delta P + [C_{11} R_3 - R_1 C_{31}] \cdot [C_{22} C_{11} - C_{12} C_{21}] \\
 & - [R_2 C_{11} - R_1 C_{21}] [C_{32} C_{11} - C_{12} C_{31}]
 \end{aligned}$$

The above equation is Eq. (4.8).

APPENDIX B. THE CALCULATION OF OVERALL  
HEAT TRANSFER COEFFICIENT

Willhite (18) suggested the following trial and error procedure to determine the overall heat transfer coefficient,  $U_o$ , for wellbore heat losses calculation.

- 1) Assume  $U_o$ .
- 2) Calculate the casing inside surface temperature:

$$T_{ci} = T_h + \frac{r_{to} U_o \ln \frac{r_h}{r_{co}}}{k_{cem}} (T_w - T_h)$$

where  $T_h$  = cement-formation interface temperature,  
 $T_w$  = wellbore inside temperature,  
 $r_{to}$  = tubing outside radius,  
 $r_h$  = radius of drill hole,  
 $r_{co}$  = casing outside radius,  
 $k_{cem}$  = thermal conductivity of cement.

- 3) Estimate heat transfer coefficient for radiation between outside tubing surface and inside casing surface.

$$h_r = \sigma F (T_w^2 + T_{ci}^2) (T_w + T_{ci})$$

where  $F = \left[ \frac{1}{\epsilon_{to}} + \frac{r_{to}}{r_{ci}} \left( \frac{1}{\epsilon_{ci}} - 1 \right) \right]^{-1}$ ,

$\epsilon$  = emissivity,

$\sigma$  = Stefan-Boltzmann constant.

- 4) Estimate heat transfer coefficient for natural convection in annulus.

$$h_c = \frac{1}{r_{to} \ln \frac{r_{ci}}{r_{to}}} \cdot k_{an} 0.049 (G_r P_r)^{0.333} P_r^{0.074}$$

where  $k_{an}$  = thermal conductivity of the fluid in annulus,

$r_{ci}$  = casing inside radius,

$P_r$  = Prandtl number,

$$G_r = \frac{(r_{ci} - r_{to})^3 g \rho_{an}^2 (T_w - T_{ci})}{(\mu_{an})^2 T_{an}}$$

$\mu_{an}$  = viscosity of the fluid in annulus,

$\rho_{an}$  = density of the fluid in annulus,

$T_{an}$  = average temperature of annulus,

$g$  = gravity.

- 5) Calculate  $U_o$ .

$$U_o = \left( \frac{1}{h_c + h_r} + \frac{r_{to} \ln \frac{r_h}{r_{to}}}{k_{cem}} \right)$$

- 6) If the assumed value and the calculated value of  $U$  do not agree, repeat the steps until agreement is obtained between two successive trials.